

Winter 2018

Offshore Wind Energy: Simulating Local Offshore Wind Turbine

Ian P. Aquino
Old Dominion University

Follow this and additional works at: https://digitalcommons.odu.edu/mae_etds

 Part of the [Mechanical Engineering Commons](#), and the [Oil, Gas, and Energy Commons](#)

Recommended Citation

Aquino, Ian P.. "Offshore Wind Energy: Simulating Local Offshore Wind Turbine" (2018). Master of Science (MS), thesis, Mechanical & Aerospace Engineering, Old Dominion University, DOI: 10.25777/yk5c-3h57
https://digitalcommons.odu.edu/mae_etds/169

This Thesis is brought to you for free and open access by the Mechanical & Aerospace Engineering at ODU Digital Commons. It has been accepted for inclusion in Mechanical & Aerospace Engineering Theses & Dissertations by an authorized administrator of ODU Digital Commons. For more information, please contact digitalcommons@odu.edu.

**OFFSHORE WIND ENERGY:
SIMULATING LOCAL OFFSHORE WIND TURBINE**

by

Ian P. Aquino
B.S. May 2011, Radford University

A Thesis Submitted to the Faculty of
Old Dominion University in Partial Fulfillment of the
Requirements for the Degree of

MASTER OF SCIENCE

MECHANICAL ENGINEERING

OLD DOMINION UNIVERSITY

December 2018

Approved by:

Ayodeji Demuren (Director)

Krishna Kaipa (Member)

Xiaoyu Zhang (Member)

Brett Newman (Member)

ABSTRACT

OFFSHORE WIND ENERGY: SIMULATING LOCAL OFFSHORE WIND TURBINE

Ian P. Aquino
Old Dominion University, 2018
Director: Ayodeji Demuren

Dominion Virginia Energy is looking at the possible creation of an offshore wind plant as a renewable source of electricity to be located off the coast of Virginia Beach. This thesis reports on a computer simulation based on local wind conditions and possible single wind turbine installation.

The National Buoy Data Center keeps records of the local wind conditions gathered in real time and available to the public. These data give a general overview of the wind conditions in Virginia Beach which is used to simulate atmospheric boundary layer (ABL) flow conditions and is subsequently used as input data for different test cases for wind turbine simulations. The program used to simulate the turbine is Simulator fOr Wind Farm Applications (SOWFA) developed by NREL. SOWFA is based on the open source CFD code OpenFoam.

With current studies and data from other wind plants, certain expectations and predictions can be made for local power generation. Local wind used in a general turbine energy output equation shows that most turbine energy is generated between 11 m/s and 12 m/s over the span of a year. The simulations created with a speed slightly over the rated speed of 11.4 m/s produced the turbines max power output of the expected 5 MW. Combining the knowledge of local data producing the majority of power at its rated speed and simulations producing 5 MW of power at this speed help confirm the importance of creating an offshore turbine.

Copyright, 2018, by Ian Aquino, All Rights Reserved.

This thesis is dedicated to the proposition that the harder you work, the luckier you get.

ACKNOWLEDGMENTS

There are many people who have contributed to the successful completion of this dissertation. I extend many, many thanks to my committee members for their patience and hours of guidance on my research and editing of this manuscript. The untiring efforts of my major advisor deserve special recognition.

TABLE OF CONTENTS

LIST OF FIGURES	ix
LIST OF TABLES	xii
CHAPTER 1 - INTRODUCTION.....	1
1.1 Overview	1
1.2 Scope of Research	2
CHAPTER 2 – LITERATURE REVIEW	4
2.1 Wind Energy	4
2.1.1 The Nature of Wind	6
2.1.2 Wind Variation by Location	7
2.1.3 Annual and Seasonal Variations	7
2.1.4 Diurnal Variations.....	8
2.1.5 Wind and Height Variation.....	8
2.1.6 Offshore Application	9
2.2 Offshore Wind Energy Review	10
CHAPTER 3 – TURBINE THEORY.....	12
3.1 Actuator Disc Concept	13
3.1.1 Momentum Theory	14
3.1.2 Power Coefficient	15
3.2 Actuator Line Model	18
3.3 Basis of Turbine Model.....	20

3.4	NREL Turbine and SOWFA	21
CHAPTER 4 – LOCAL WEATHER CONDITIONS		25
4.1	NOAA Data explained	25
4.1.1	NOAA wind data	27
CHAPTER 5 – RESULTS		30
5.1	Precursor.....	30
5.2	Turbine Simulations	36
5.2.1	Axial Velocity.....	39
5.2.2	Tangential Velocity.....	43
5.2.3	Velocity Magnitude	46
5.2.4	Alpha.....	48
5.2.5	Coefficient of Drag	51
5.2.6	Coefficient of Lift	54
5.2.7	Drag.....	56
5.2.8	Lift.....	58
5.2.9	Axial Force.....	60
5.2.10	Tangential Force	62
5.2.11	Power Generator	64
5.2.12	Wake Profiles.....	67
5.3	Wind Plant.....	70

5.3.1 Axial Velocity.....	71
5.3.2 Alpha.....	72
5.3.3 Drag.....	73
5.3.4 Lift.....	74
5.3.5 Power Generator	75
5.3.6 Wake Profiles.....	77
CHAPTER 6 - CONCLUSION	79
6.1 Improvements.....	79
6.2 Suggestions for Future Work	80
REFERENCES	81
APPENDIX A.....	85
VITA.....	89

LIST OF FIGURES

Figure 2-1. Power in the Wind.....	6
Figure 2-2. Average wind speed by month.....	8
Figure 3-1. An Energy Extracting Actuator Disc and Stream-tube.....	13
Figure 3-2. Variation of C_p and C_T with Axial Induction Factor a	17
Figure 3-3. Cross-sectional airfoil element showing velocity and force vectors.....	18
Figure 3-4. Actuator points and data points along turbine blade.....	23
Figure 4-1. Location of anemometer used for local wind data.....	25
Figure 4-2. Wind Speed Distribution.....	28
Figure 4-3. Estimated power generated distribution.....	28
Figure 5-1. Contours of velocity magnitude of simulated ABL.....	31
Figure 5-2. Time-averaged simulated velocity vs elevation z for 3.4m/s.....	32
Figure 5-3. Time-averaged simulated velocity vs elevation z for 5.2m/s.....	33
Figure 5-4. Time-averaged simulated velocity vs elevation z for 9.6m/s.....	33
Figure 5-5. Mean temperature for simulation using 3.4m/s as initial velocity.....	34
Figure 5-6. Mean temperature for simulation using 5.2m/s as initial velocity.....	35
Figure 5-7. Mean temperature for simulation using 9.6m/s as initial velocity.....	35
Figure 5-8. Contours of velocity magnitude at $t=12000$ seconds.....	36
Figure 5-9. Contours of the time-averaged velocity magnitude.....	36
Figure 5-10. Contours of pressure averaged over time.....	37
Figure 5-11. Azimuth for 6.2 m/s inflow.....	38
Figure 5-12. Azimuth positions.....	39

Figure 5-13. Direction of axial velocity in relation to the turbine	40
Figure 5-14. Computed averaged axial velocity along blade	41
Figure 5-15. Computed axial velocity of blade tip averaged along azimuth	42
Figure 5-16. Computed average tangential velocity along blade	43
Figure 5-17. Computed tangential velocity of blade tip averaged along azimuth	44
Figure 5-18. A) Blade position at 90° B) Blade position at 270°	45
Figure 5-19. Computed average velocity magnitude along blade	46
Figure 5-20. Computed velocity magnitude of blade tip averaged along azimuth	47
Figure 5-21. Computed averaged alpha along blade	49
Figure 5-22. Computed alpha of blade tip averaged along azimuth	50
Figure 5-23. Cylinder1 and Cylinder2 reference point	51
Figure 5-24. Computed averaged Cd along blade	52
Figure 5-25. Computed Cd of blade tip averaged along azimuth	53
Figure 5-26. Computed averaged Cl along blade	54
Figure 5-27. Computed Cl of blade tip averaged along azimuth	55
Figure 5-28. Computed average drag along blade	56
Figure 5-29. Computed drag of blade tip averaged along azimuth	57
Figure 5-30. Computed averaged lift along blade	58
Figure 5-31. Computed lift of blade tip averaged along azimuth	59
Figure 5-32. Computed averaged axial force along blade	60
Figure 5-33. Computed axial force of blade tip averaged along azimuth	61
Figure 5-34. Computed averaged tangential force along blade	62
Figure 5-35. Computed tangential force of blade tip averaged along azimuth	63

Figure 5-36. Computed power generated over time	64
Figure 5-37. Power generated averaged along azimuth.....	65
Figure 5-38. Turbine wake profile at constant inflow of 4.1m/s	67
Figure 5-39. Turbine wake profile at constant inflow of 6.2m/s	68
Figure 5-40. Turbine wake profile at constant inflow of 11.6m/s	69
Figure 5-41. Contours of Wind plant simulation for velocity 5.4 m/s.....	70
Figure 5-42. Axial velocity of blade tip averaged along azimuth.....	71
Figure 5-43. Alpha of blade tip averaged along azimuth.....	72
Figure 5-44. Drag of blade tip averaged along azimuth	73
Figure 5-45. Lift of blade tip averaged along azimuth	74
Figure 5-46. Power Generated over time.....	76
Figure 5-47. Wake profile with velocity of 3.4 m/s with an elevation of 27.9 m.....	77
Figure 5-48. Wake profile with velocity of 5.2 m/s with an elevation of 27.9 m.....	78
Figure 5-49. Wake profile with velocity of 9.6 m/s with an elevation of 27.9 m.....	78

LIST OF TABLES

Table 3-1. Properties of the NREL 5-MW Baseline Wind Turbine	21
Table 3-2 Distributed Blade Aerodynamic Properties.....	22
Table 5-1	66
Table 5-2.....	76

CHAPTER 1

INTRODUCTION

1.1 Overview

In the past, offshore wind turbines may have not been a cost efficient way of providing energy. Now, with cheaper and more efficient technology used for wind energy is becoming more available, it is worth looking into the use of offshore wind energy. Dominion Virginia Energy is looking to the production of offshore wind power by creating a wind farm off the coast of Virginia Beach [1]. Currently, there is only one operational offshore wind farm in the United States, and it is located in the Rhode Island. The Wind Block Island Wind Farm in Rhode Island started operations in December 2016 and uses five Alstom Haliade 150-6MW turbines to create a 30MW offshore wind farm [2]. The offshore wind plant (wind plant and wind farm are interchangeable terms) for Virginia is currently in planning, with installation targeted to be completed by 2020. It will be two 6MW turbines installed next to each other 27 miles off the coast of Virginia Beach [1]. To get a better understanding of the local conditions that affect offshore wind energy production, a program called Simulator fOr Wind Farm Applications (SOWFA) will be used to simulate the turbines interaction with the local atmospheric boundary condition.

SOWFA is a simulator for wind farm applications that currently uses CFD tools based on OpenFOAM. It is coupled with NREL's FAST wind turbine/system dynamic models. This was created to be an open-source simulator with the ability to include other modules [3].

OpenFOAM has been shown to be a fairly accurate solver for ABL simulations, making it an ideal choice for this application because it is flexible, open source, and available at no cost [4].

Generally, SOWFA requires creating three different simulations. The first one creates a 3D mesh in a three dimensional domain where it uses the input data such as wind speed, direction, temperature, and others to form the ABL (Atmospheric Boundary Layer) results for that space. This is referred to as the Precursor in SOWFA. The second simulation allows for the manipulation or change of the turbine used for the wind plant. This is called the Turbine simulation, and it allows for the simulation of the wind turbine in a smaller grid using data separate from the ones obtained from the Precursor. Using an isolated wind turbine allows the user to verify that the turbine is producing expected results. The final one incorporates aspects from both simulations mentioned previously. The Wind Farm simulation uses the data from the precursor as the input data to populate the domain used in the wind plant grid. It also places the desired turbine in a specified location for the precursor data to interact with the turbine blades [3].

1.2 Scope of Research

There are plenty of ways to come up with estimates of power generation of a turbine in simple conditions. The simplest of cases is one where the wind turbine has fairly constant wind direction and speed. This starts to get more complicated with the addition of wind turbines since the leading turbine creates a wake behind it reducing the energy trailing turbines can extract. Multiple turbines in the windfarm with the addition of changing wind conditions can make understanding the local conditions' effects on the windfarm difficult.

The purpose of this research is to successfully simulate and understand basic cases of a single wind turbine and compare to expected results. This single wind turbine simulation is a necessary step to creating a wind farm simulation as it confirms the simulation works under desired conditions and gives a better understanding when designing the other parameters for the wind farm. The objectives of this study include.

- 1) Making any necessary fixes to the SOWFA code to make it work with OpenFOAM 2.0.1.

This problem has arisen due to the fact that SOWFA is an open source program where certain fixes were not documented for different versions of OpenFOAM.

- 2) Extract local wind data from the National Data Buoy Center data collection for local conditions. Once the data is collected, it will need to be organized into a usable format that can be used in SOWFA simulations.
- 3) Create a few different scenarios where each simulation has varied wind speed and direction. Each of these simulations will be split and analyzed in the Precursor, Turbine, and Wind Farm portion of their simulation.

CHAPTER 2

LITERATURE REVIEW

With plenty of studies having been done, there can be some general expectations when it comes to the decision to use wind for energy. There often are trends when it comes to the nature of wind for each specific location even if they differ from each other. These trends can be variables such as the season and time of day. This knowledge can be a very useful tool when deciding if wind energy is a reasonable and cost effective move for the future.

2.1 Wind Energy

There are plenty of difficulties when deciding if wind energy is a practical and cost effective method of producing energy, but there are also patterns and known processes for creating an informed decision. Useful information to estimate would be the wind power output.

The wind turbine's power output is given by the expression

$$P = \frac{1}{2} C_p \rho A U^3 \quad 2.1.1$$

where C_p is the power coefficient, ρ is the density of air (1.225 kg/m^3), A is the rotor swept area, and U is wind speed. The power coefficient describes the fraction of power that can be converted to mechanical energy from the wind. There is a theoretical maximum called the Betz Limit with a value of 0.593 [5, p. 6]. The two main factors for increasing power output is through using a location with higher wind speeds or by increasing the swept area of rotor [5, p. 7].

As can be seen from Equation 2.1.1, a doubling of the rotor diameter would lead to a four-time increase in power. Also, it can be seen that a doubling of wind speed would lead to an eight-fold increase of power. This has led to wind farm development to be located in areas with higher wind speeds.

Although wind speed is the greatest factor for generating power, there are other factors that can be taken into account, such as air density. Air density will change depending on temperature and elevation. A turbine will usually produce more power in the winter than the summer for the same wind speeds [6].

The wind turbine must cover a large range of different wind speeds. For instance, the theoretical NREL 5 MW turbine cuts in at 3 m/s and cuts out at 25 m/s to prevent damage [7]. This corresponds to a much larger range of intercepted power than can be converted to energy. For example, if the cut-in speed is 4 m/s and the cut-out speed is 24 m/s, the 6 to 1 wind speed corresponds to a 216 to 1 range of intercepted power. This means that a short period of strong wind will contribute a lot more than a constant breeze over a long period. In other words, one hour of a severe gale will have as much energy as 216 hours of a moderate breeze. Plant locations are often discussed in terms of their mean wind speed, but the variability of speed is also an important factor. Sites that are gusty will generally produce more energy than ones with constant wind with the same average wind speed over the year [6, p. 32]. Figure 2-1 shows a better understanding of the cubic relationship between wind speed and power.



Figure 2-1. Power in the Wind

2.1.1 The Nature of Wind

Wind energy is subject to a large range of variability. This includes spatial and temporal variability in small and large scales. For spatial variability, it refers to the fact that there are many regions in the world that are different geographically with very different wind conditions. Temporal variability can be predictable for certain time scales while unpredictable in others. With short time-scales, it is not easy to predict more than a few days in advance, but for even shorter time-scales, there may be predictable patterns called diurnal variations depending on the locations. For longer periods shorter than a year, seasonal variations can be predictable, but for long-term scales that may span over a decade or more, there may be a large variations [5, p. 11]. This is not well understood, which can make it difficult for predicting the economic viability of a wind-farm.

2.1.2 Wind Variation by Location

The differential heating of the earth's surface is the main driving force behind wind. The warm air rises then circulates in the atmosphere where it will sink back down to a cooler location. This large scale motion is largely affected by the earth's rotation [5, p. 12]. This results in global circulation patterns that lead to known patterns like the trade winds. The global pattern is affected by the non-uniform surface of the earth, such as oceans and land masses. This causes the global circulation patterns to be disturbed by smaller scale variation on the continental scale. All of these complex interactions are what lead to the day to day unpredictability of the weather. Even though the weather in particular locations can be unpredictable, underlying tendencies lead to the different climates between regions. Topography will also have an impact on the climate differences.

Coastal regions tend to be windy because of the differential heating between land and sea. When the sea is warmer than the land, the wind circulates the colder air from the land to the warmer sea before it rises over the water and cools back down over land. This pattern is reversed when the land is warmer. This pattern tends to reverse over a 24 hour cycle because the land heats up and cools down quicker than the surface of the sea [5, p. 13].

2.1.3 Annual and Seasonal Variations

Most locations will experience variations of wind speed over the period of the year. For example, local NOAA measurements (Figure 2-2) on the coast of Norfolk show that during the summer months, the wind speeds tend to be at their lowest and start to increase during the fall, staying there till early spring when it starts to decrease leading up to the summer [8].

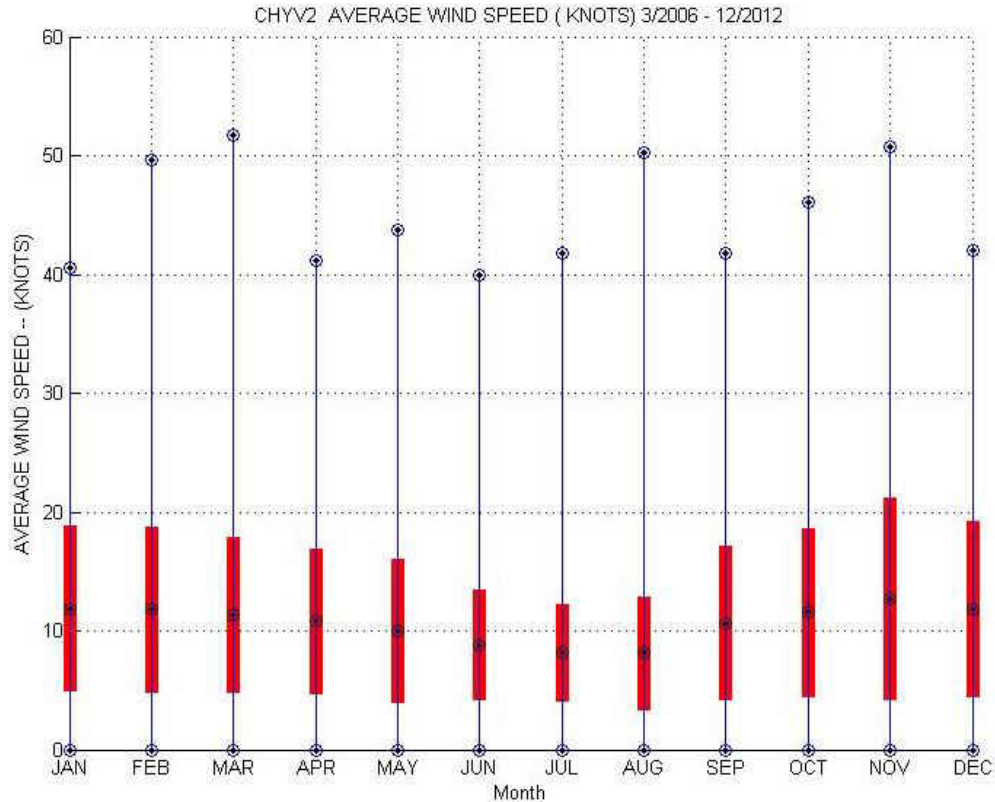


Figure 2-2 Average wind speed by month

2.1.4 Diurnal Variations

There also tend to be systematic variations in the wind during the day. This is driven by the differential heating from the sun and rotation of the earth. This tends to make the winds stronger during the day than the night. These diurnal effects depend greatly on proximity to the ocean and the local geography [6, pp. 38-39].

2.1.5 Wind and Height Variation

In general, the higher the turbine the better due to the fact that wind strength increases with height. Another benefit may be that the stresses that turbulence can cause tend to decrease with

higher turbines. This average increase in wind speed can be approximated by using the power law:

$$\frac{U}{U_0} = \left(\frac{h}{h_0}\right)^\alpha \quad 2.1.2$$

where U is the speed at the height h , and U_0 is the speed and a reference height of h_0 . The power law exponent that depends on surface roughness is represented by α . The exponent α increases with rougher surfaces; for example, calm seas can be a value of around 0.1, while landscapes with trees and hedges can be around 0.3 [6, p. 36]. We can see from the equation that raising the height of the turbine as much economically possible is beneficial, especially over rough surfaces. A value of 0.14 for α is the default estimate used in North America [6, p. 37].

2.1.6 Offshore Application

When using the power law to predict the benefits of raising the hub height, the standard value of 0.14 for α is often used [6, p. 36]. Unlike the land, the roughness of the sea is dependent on wave height and patterns. A range of 0.1 to 0.2 usually covers most of the offshore sites. For offshore sites, it is very difficult to predict the wind shear for a particular site. One factor that makes this difficult is that the roughness of the sea surface depends on the wave conditions, which depends on the wind conditions. Another factor is that there is often a delay between the changes in wind speed versus the changes in wave height and pattern. The seasonal differences in temperature between air and water has an effect on wind shear [6, p. 158].

Turbulence intensity at sea can often be less than that on land because of a lower surface roughness. Even though turbulence can exert more stress on turbine blades and

structures it can reduce the wake lengths which in turn would reduce array losses from upstream neighbors [6, p. 159].

2.2 Offshore Wind Energy Review

With the increased interest in offshore wind energy, there are a variety of studies related to this subject. Areas of interest include ABL's effect on turbines, turbine array placement, turbine wakes, and plenty of other related topics. These efforts have been important for moving towards renewable energy, where through simulations and calculations, offshore energy has been shown to be a reasonable place for energy production in the Mid-Atlantic region [9]. Other offshore energy generation studies have been done well for the Atlantic [10]. Of course there are plenty of other locations other than the Atlantic where simulations were modeled for, such as the one done by Christos [11].

Wake studies are important in offshore wind energy because the trailing turbines will produce less energy, and the placement and distance from leading turbines will be important factors in making the wind plant as efficient as possible. There is also surface roughness and atmospheric stability which can have important effects on wind turbines power production, wake, and structural response [12]. Other numerical computation studies, such as one by Ivanell, give a better understanding of wakes generated by turbines [13]. Another simulation has included looking at how the alignment of the wind plant affects the average power output of the windfarms, which has shown in a single inflow direction that a staggered (row 1 and row 3 are aligned) set up would not produce the most power [14]. This topic of layout optimization has been simulated by others as well [15].

Using measurement-driven data can also be useful when trying to create simulations local to an area of interest. This approach also allows the comparison of the simulation to measure turbine performance in that location. Using measurement-driven data, Quon et al. were able to accurately show that SOWFA could capture the performance loss of the trailing turbine [16].

Another important direction offshore studies are going is in the cost-effectiveness of using offshore energy. An important aspect for this is understanding the loading fatigue on turbines in turbulent conditions produced by wake of leading turbines. These turbulent conditions increase the loads on the turbine [17]. Types of turbine may also increase loading such a floating turbines needed for deep water [18]. Turbine load studies can be key in understanding the life cycle of the turbines and ways to improve its efficiency.

There are plenty of other areas that are being studied in respect to offshore energy such as yaw control and pitch control [19] [20]. With offshore wind energy gaining importance the understanding around many of these concepts will continue to improve and lead to more efficient offshore wind plants.

CHAPTER 3

TURBINE THEORY

A wind turbine works by extracting the kinetic energy from wind. The removal of kinetic energy will cause the wind to slow down. Only the air that passes through the rotor disk will be affected and can be assumed that the air mass that passes through the disc remains separate from the air that doesn't pass through the rotor disc. This forms a long stream tube where the mass flow rate will be the same along all stream-wise positions. Since the air in the stream tube slows down without being compressed, the cross-sectional area of the stream tube expands. This is to accommodate the slower air [5, p. 41].

Wind turbines are designed to extract pressure energy in a step-like manner, because a sudden step change in velocity is not possible due to the enormous forces it would require. As the air travels towards the turbine, it gradually slows before reaching the rotor disc. By the time the air arrives at the rotor disk, it is already at a lower velocity than the free stream wind. Because its kinetic energy has already decreased before any work has been done on the air, its static pressure rises.

When the air passes through the rotor disc it causes a drop in static pressure. This air that is traveling downstream, called the wake, will have lower speed and static pressure. Far downstream the static pressure will increase back up to that of the atmospheric level to reach equilibrium. This increase in static pressure decreases the kinetic energy even more leading to an even further decrease in wind speed. The wake far downstream will thus have the same static pressure as far upstream but with a decrease in kinetic energy [5, p. 42].

3.1 Actuator Disc Concept

Without any specific turbine design, the energy extraction process can still be analyzed. The device used for this process is called an actuator disc, which can be seen in Figure 3-1. In order for the mass flow rate to be equal along the stream-tube the cross-sectional area of the stream-tube will be smaller upstream and larger downstream.

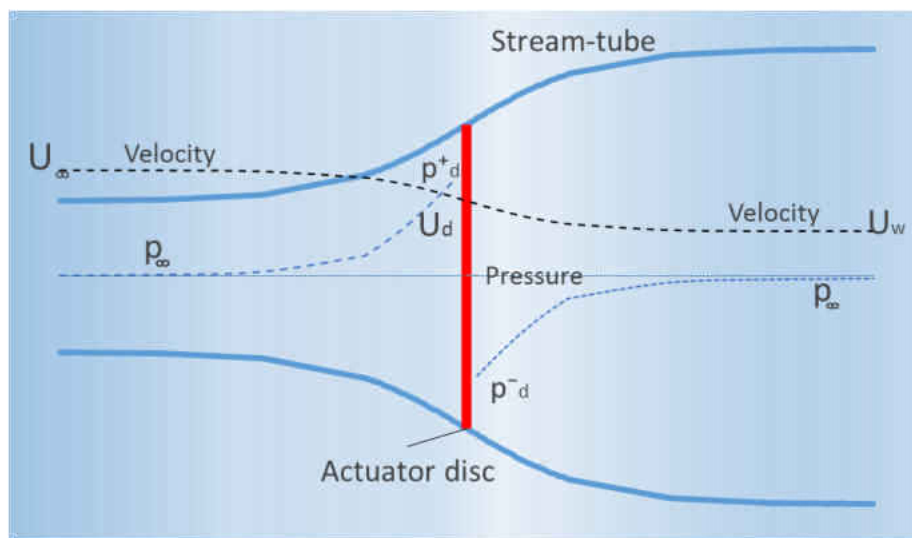


Figure 3-1. An Energy Extracting Actuator Disc and Stream-tube

The mass flow rate along the stream-tube can be represented by Equation 3.1.1, since the mass flow rate is the same everywhere along the stream-tube

$$\rho A_\infty U_\infty = \rho A_d U_d = \rho A_w U_w \quad 3.1.1$$

The mass of air in a unit length of time is ρAU , where ρ is air density, A is the cross-sectional area and U is the flow velocity. The subscripts ∞ , d , and w refer to conditions far upstream, conditions at the disc, and condition in the far wake respectively.

The actuator disc induces a velocity variation that must be imposed in the free-stream velocity. The induced flow at the disc is given by $-aU_\infty$, where a is the axial flow induction factor. This gives a net stream-wise velocity at the disc

$$U_d = U_\infty(1 - a) \quad 3.1.2$$

A constantly loaded actuator disc, in which the forces representing a rotor are prescribed and distributed on a permeable disc of zero thickness, is the simplest formulation of this model. This approach has been used in order to validate the assumptions underlying the momentum theory [21]. It has also been used for giving information about fundamental features of axisymmetric wakes, including unsteady wake states [22]. Other more recent studies have used a constant loaded actuator disc in combination with a large eddy simulation of the flow field to study the properties of the Reynolds stresses [23].

3.1.1 Momentum Theory

When the air passes through the disc, it goes through a change in velocity. The change in velocity $U_\infty - U_w$ times the mass flow rate equals the change in momentum

$$\text{Rate of change of momentum} = (U_\infty - U_w)\rho A_d U_d \quad 3.1.3$$

The pressure difference across the disc is the force behind the change in momentum. This is because the stream-tube is surrounded by air at atmospheric pressure which gives a net force of zero. Therefore,

$$(p_d^+ - p_d^-) A_d = (U_\infty - U_w)\rho A_d U_\infty(1 - a) \quad 3.1.4$$

The pressure difference ($p_d^+ - p_d^-$) can be obtained by applying Bernoulli's equation to the upstream and a downstream sections of the stream tube separately. The reason separate equations are necessary is because the total energy upstream is different than downstream. For a unit volume of air,

$$\frac{1}{2}\rho U^2 + p + \rho gh = \text{constant} \quad 3.1.5$$

so upstream will be

$$\frac{1}{2}\rho_\infty U_\infty^2 + \rho_\infty gh_\infty = \frac{1}{2}\rho_d U_d^2 + p_d^+ + \rho_d gh_d \quad 3.1.6$$

Assuming the flow is incompressible ($\rho_\infty = \rho_d$) and the horizontal ($h_\infty = h_d$) then upstream will be

$$\frac{1}{2}\rho U_\infty^2 + \rho_\infty = \frac{1}{2}\rho U_d^2 + \rho_d^+ \quad 3.1.7$$

and downstream will be

$$\frac{1}{2}\rho U_w^2 + \rho_\infty = \frac{1}{2}\rho U_d^2 + \rho_d^- \quad 3.1.8$$

Subtract these two equations

$$(\rho_d^+ - \rho_d^-) = \frac{1}{2}\rho(U_\infty^2 - U_w^2) \quad 3.1.9$$

Equation 3.1.4 then gives

$$\frac{1}{2}\rho(U_\infty^2 - U_w^2)A_d = (U_\infty - U_w)\rho AU_\infty(1 - a) \quad 3.1.10$$

so

$$U_w = (1 - 2a)U_\infty \quad 3.1.11$$

3.1.2 Power Coefficient

From Equation 3.1.4, the force on the air becomes

$$F = (\rho_d^+ - \rho_d^-)A_d = 2\rho A_d U_\infty^2 a(1 - a) \quad 3.1.12$$

Since this force is concentrated on the actuator disc, the rate of work done by this force is FU_d giving the power extraction from the air

$$Power = FU_d = 2\rho A_d U_\infty^3 a(1-a)^2 \quad 3.1.13$$

This defines the power coefficient as

$$C_p = \frac{Power}{\frac{1}{2}\rho U_\infty^3 A_d} \quad 3.1.14$$

where the denominator represents the available power in the air in the absence of the actuator disc. Therefore,

$$C_p = 4a(1-a)^2 \quad 3.1.15$$

The maximum value of C_p occurs when

$$\frac{dC_p}{da} = 4(1-a)(1-3a) = 0 \quad 3.1.16$$

which makes $a = \frac{1}{3}$. Hence,

$$C_{pmax} = \frac{16}{27} = 0.593 \quad 3.1.17$$

Using Equation 3.1.12, the force on the actuator disc that is caused by the pressure drop can also be non-dimensionalized to give a Coefficient of Thrust:

$$C_T = \frac{F}{\left(\frac{1}{2}\rho U_\infty^2 A_d\right)} \quad 3.1.18$$

$$C_T = 4a(1 - a) \quad 3.1.19$$

When $a \geq \frac{1}{2}$, a problem occurs because the wake velocity $(1 - 2a)U_\infty$ becomes 0 or negative. In these conditions the momentum theory will no longer work, and some modifications need to be made [5]. Figure 3-2 shows the variation of the power coefficient and thrust coefficient with a . The dashed lines represent where the conditions mentioned no longer work.

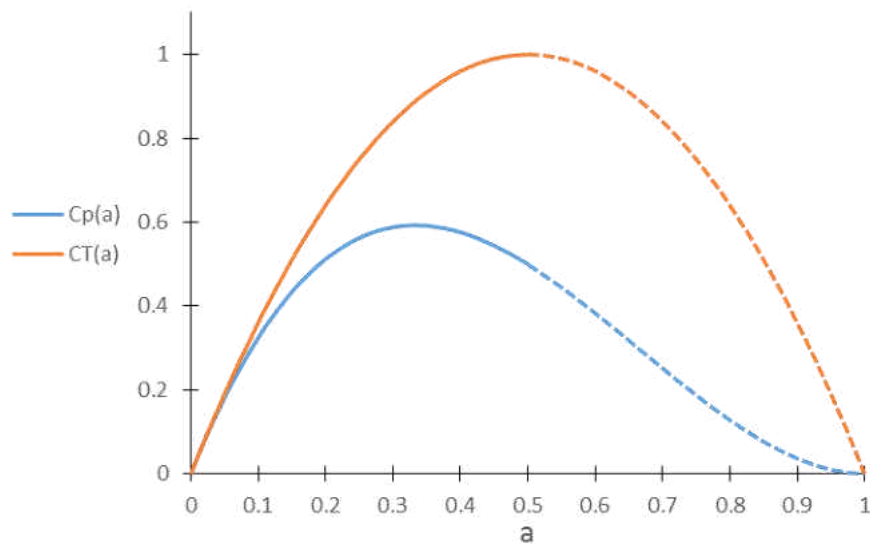


Figure 3-2 Variation of C_p and C_T with Axial Induction Factor a

3.2 Actuator Line Model

The Actuator Line Model uses discrete sections with its respective properties and airfoil to simulate the turbine's set points along each blades axis [24]. It uses the local wind speed and angle of attack to calculate the lift and drag at each point. Figure 3-3 shows the cross-sectional airfoil at some definable radius along the blade. Skipping ahead, Figure 3-4 shows an example of how the points may be arranged for the actuator line model.

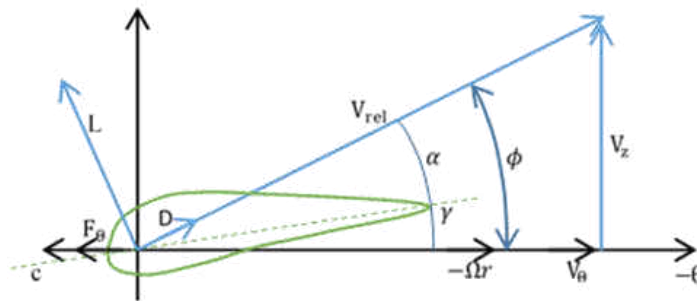


Figure 3-3. Cross-sectional airfoil element showing velocity and force vectors

The local velocity relative to the rotating blade is determined by

$$V_{rel} = \sqrt{V_z^2 + (\Omega r - V_\theta)^2} \quad 3.2.6$$

In this equation, V_z represents the velocity in the axial direction, and V_θ represents the tangential wind velocity. Here, Ω denotes the angular velocity. In these turbine simulations, the inflow is constant and all coming from the axial direction, meaning that V_z should be small compared to Ω along the tip of the blade and would make a bigger difference as it gets closer to the center.

The local angle of attack is given by

$$\alpha = \varphi - \gamma \quad 3.2.7$$

where γ represents the local pitch angle, and the flow angle between V_{rel} and the rotor plane is determined by

$$\varphi = \tan^{-1} \frac{V_z}{\Omega r - V_\theta} \quad 3.2.8$$

Knowing the values of the angle of attack the lift and drag can be calculated using

$$L = \frac{1}{2} C_L(\alpha) \rho V^2 c w \quad 3.2.9$$

$$D = \frac{1}{2} C_D(\alpha) \rho V^2 c w \quad 3.2.10$$

$C_L(\alpha)$ and $C_D(\alpha)$ are obtained from predetermined values based off experimental data for the specific turbine being used in simulations (these simulations use Appendix A for $C_L(\alpha)$ and $C_D(\alpha)$). Where $C_L(\alpha)$ and $C_D(\alpha)$ are the lift coefficient and drag coefficient, respectively. While V is the velocity magnitude, ρ is the density, c is the chord, and w is the width of the section.

Sørensen and Shen use a Gaussian projection to project the force calculated at the actuator line points onto the CFD grid as a body force [25]. F_i^A is the actuator element force, r is the distance between CFD cell center and actuator point, and ε controls Gaussian width. f_i^T is the force normalized and projected back to the flow in Equation 3.4.1 described later.

$$f_i^T(r) = \frac{F_i^A}{\varepsilon^3 \pi^{3/2}} \exp \left[- \left(\frac{r}{\varepsilon} \right)^2 \right] \quad 3.2.11$$

The benefit of the actuator line model is that fewer grid points are needed when using airfoil data compared to using the actual geometry to simulate the influence of the blades. This allows for a detailed study of the different wake structures such as tip and root vortices while using a reasonable number of grid nodes.

3.3 Basis of Turbine Model

To be able to generate useful data for the study, use of a realistic turbine is necessary. The Department of Energy's (DOE's) National Renewable Energy Laboratory (NREL) sponsored a conceptual study to assess offshore wind technology. One of the specifications created for their study is the "NREL offshore 5-MW baseline wind turbine". When creating the baseline turbine, the first aspects taken into consideration were size and power rating needed for an offshore wind turbine. Based on previous studies, in order for the turbine to be cost effective the turbine had to be rated 5-MW or higher [26]. Conceptual models that were used in WindPact, RECOFF and DOWEC projects help create a composite by using the best available data.

For the development of the NREL 5-MW the data from the DOWEC study played the biggest role. The Repower 5M has a rotor radius of about 63 m. With the radius being a 63 m, it was decided to use a hub height of 90 m to give a 15 m air gap. Other properties for the NREL 5-MW baseline wind turbine can be found in the table below [7].

Table 3-1. Properties of the NREL 5-MW Baseline Wind Turbine

Rating	5 MW
Rotor Orientation, Configuration	Upwind, 3 Blades
Control	Variable Speed, Collective Pitch
Drivetrain	High Speed, Multiple-Stage Gearbox
Rotor, Hub Diameter	126 m, 3 m
Hub Height	90 m
Cut-In, Rated, Cut-Out Wind Speed	3 m/s, 11.4 m/s, 25 m/s
Cut-In, Rated Rotor Speed	6.9 rpm, 12.1 rpm
Rated Tip Speed	80 m/s
Overhang, Shaft Tilt, Precone	5m, 5°, 2.5°
Rotor Mass	110,000 kg
Nacelle Mass	240,000 kg
Tower Mass	347,000 kg
Coordinate Location of Overall CM	(-0.2 m, 0.0 m, 64.0 m)

The swept area of this turbine is $12,445.3 \text{ m}^2$. This value takes into account of the blades precone which reduce the total swept area.

3.4 NREL Turbine and SOWFA

The actuator line model in SOWFA implements three separate blades with constant geometric values according to its radius along the blade as seen in Table 3-2. This table represent actuator points of the NREL turbine and which airfoil each point will be used for the simulation. For example, if a simulation point is 40 meters from the center of the turbine, it will use the closest actuator point at 40.45 meters as a reference point. This means that the chord length will 3.256 meters and the twist of the blade will be 4.188 degrees. It will also use the properties of DU21_A17, which can be seen in the appendix Figure A-5.

Table 3-2 Distributed Blade Aerodynamic Properties

radius(m)	c(m)	twist(deg)	airfoil
2.8667	3.542	13.308	Cylinder1
5.6	3.854	13.308	Cylinder1
8.3333	4.167	13.308	Cylinder2
11.75	4.557	13.308	DU40_A17
15.85	4.652	11.48	DU35_A17
19.95	4.458	10.162	DU35_A17
24.05	4.249	9.011	DU30_A17
28.15	4.007	7.795	DU25_A17
32.25	3.748	6.544	DU25_A17
36.35	3.502	5.361	DU21_A17
40.45	3.256	4.188	DU21_A17
44.55	3.01	3.125	NACA64_A17
48.65	2.764	2.319	NACA64_A17
52.75	2.518	1.526	NACA64_A17
56.1667	2.313	0.863	NACA64_A17
58.9	2.086	0.37	NACA64_A17
61.6333	1.419	0.106	NACA64_A17

As can be seen, there are different airfoil values for the turbine along the blade. Even though there are only 17 actuator points along the radius of the blade, the simulation calculates multiple points for each actuator point as in rotates as seen in Figure 3-4. For blade 1, the blue dots show all the data points that are calculated along the turbine blade, while the red dots represent the actuator points along the radius. This also applies to blade 2 and blade 3. Also, in SOWFA the starting position of blade 1 is at 0 degrees which is represented in Figure 3-4 Actuator points and data points along turbine blade.

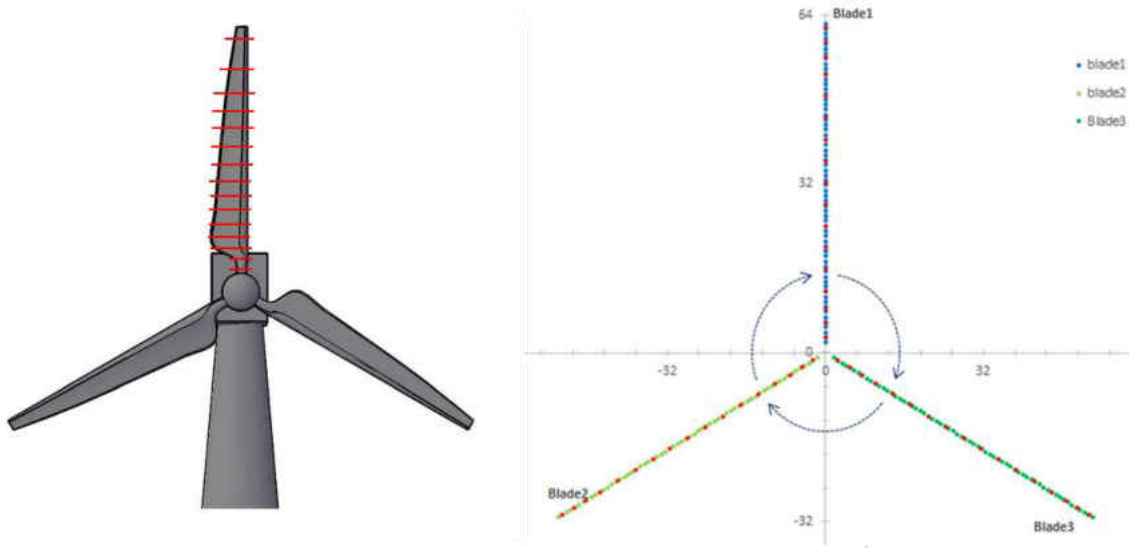


Figure 3-4 Actuator points and data points along turbine blade

The SOWFA simulations implement the actuator line model to simulate the turbine. The actuator line method helps resolve some of the problems with the actuator disc method mentioned earlier. The main limitation of the actuator disc method is that it assumes rotationally symmetric flow conditions and is not very effective in capturing the influence of tip vortices. The actuator line model distributes the loads along lines that represent blades in a 3-dimensional domain.

SOWFA implements a set of equations such as the momentum transport in Equation 3.4.1.

$$\frac{\partial \bar{u}_i}{\partial t} + \frac{\partial}{\partial x_j} (\bar{u}_j \bar{u}_i) =$$

$$-2\varepsilon_{i3k} \Omega_3 \bar{u}_k - \frac{\partial \bar{p}}{\partial x_i} - \frac{1}{\rho_0} \frac{\partial}{\partial x_i} \bar{p}_0(x, y) - \frac{\partial}{\partial x_j} (\tau_{ij}^D) - \frac{gz}{\rho_0} \frac{\partial}{\partial x_i} \rho_b + \frac{1}{\rho_0} f_i^T$$

3.4.1

Potential temperature transport

$$\frac{\partial \bar{\theta}}{\partial t} + \frac{\partial}{\partial x_i} (\bar{u}_j \bar{\theta}) = - \frac{\partial}{\partial x_j} (q_j) \quad 3.4.2$$

To account for the buoyancy effects caused by variable density the Boussinesq approximation is used. The ratio of “buoyant density” to constant density is

$$\frac{\rho_k}{\rho_0} = 1 - \left(\frac{\bar{\theta} - \theta_0}{\theta_0} \right) ; \quad \theta_0 = 300K \quad 3.4.3$$

The rotation of the planet creates the Coriolis Force. The simulation has +x as east, +y as north and +z being up. Ω_j is the rotation rate vector at a location on the planet’s surface. ϕ represents the latitude and ω is the planet’s rotation rate.

$$-2\varepsilon_{ijk}\Omega_j\bar{u}_k \quad ; \quad \Omega_j = \omega \begin{bmatrix} 0 \\ \cos\phi \\ \sin\phi \end{bmatrix} \quad 3.4.4$$

SOWFA uses these equations for simulating the atmospheric boundary layer and implements the actuator line model to simulate the forces applied to the turbine. The force simulated on the actuator points along the blade creates an equal and opposite force against the wind which is represented by the last terms $(\frac{1}{\rho_0} f_i^T)$ effect on the momentum equation (3.4.1).

This creates a wake that is affected by the forces on each actuator point on the turbine.

CHAPTER 4

LOCAL WEATHER CONDITIONS

4.1 NOAA Data explained

The data used for simulating the turbine wind were obtained from the National Buoy Data Center. The anemometer is located on the shore of Norfolk (Figure 4-1) near the mouth of the Chesapeake Bay (36.926 N 76.007 W). The height of the anemometer is 27.9 meters above the sites elevation. The planned position of the Virginia offshore turbines is around 27 miles away from land and would be near the red buoy of the image below. That buoy off the coast of Virginia does not have an anemometer on it and is unable to record wind speed. Because the offshore buoys do not have anemometers, the closest station with the necessary data was used as the reference point for the local wind data [27].

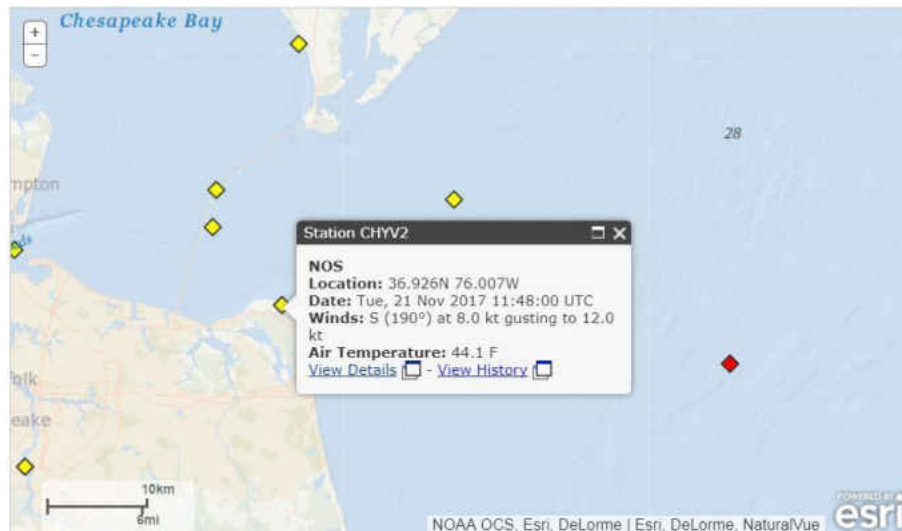


Figure 4-1. Location of anemometer used for local wind data

The measurements that the anemometer at this location records are WDIR (wind direction), WSPD (wind speed), GST (gust speed), and ATMP (air temperature). The wind direction is measured in degrees clockwise from true north in which the wind is coming from. Wind speed is averaged over a 6-minute period [28].

There are two methods used to calculate the average wind speed and direction [29].

- 1) The first method for averaging wind is applied to the measurements that are reported from DACT, VEEP, and ARES payloads. The average wind speed is the simple scalar average of the wind speed observations. A “unit-vector” average is used to calculate the average wind direction. Unity serves as the length of the vector, and the wind direction serves as the orientation of the vector. Then u and v components are computed and the average wind direction is derived from $\arctan(u/v)$. This technique will produce greater wind speeds than if a true vector average was used.
- 2) The second method used to calculate the average wind speed and direction that is reported by NDBC’s older GSBP payloads are a true vector average. In this method, the magnitude of the vector is represented by the wind speed observation and the direction observations are used for the orientation. The vectors are then broken down into their u and v components then averaged separately. The resulting average speed and direction are calculated from the Pythagorean Theorem and $\arctan(u/v)$ respectively.

Gust speed is measured by 5 to 8 second peaks during the 6 minute period. And air temperature is measure in Celsius [28].

4.1.1 NOAA wind data

When predicting wind speed over the course of a year, it has been helpful for many cases to characterize it in a probability distribution. If not much data has been collected, probability distributions such as the Weibull distribution are used to represent the possible variation in an hourly mean of wind speed over the year [5, p. 14]. In this case, using a probability distribution is not needed because for this study there has been plenty of measurements taken along the coast. Within the year represented by this distribution table there are about 100 hours missing from the data. Factors such as equipment failure are likely to blame for some of the gaps in the data. These data have been slightly modified to try to better predict the power output of the turbine over the year. For the wind distribution the Power Law has been used to make up for the relatively low elevation of the anemometer of 27.9 meters to about 90 meters. For Figure 4-2 and Figure 4-3, the wind speed has been distributed in bins of 1m/s intervals. This allows for good but simple estimates of the possible power generated by the turbine at the specified location. Now by only looking at the wind distribution (Figure 4-2) it may seem that the turbine would not produce a lot of energy since the wind speed spends most of the time between 4 to 6 m/s. This may lead one to assume that this range is where most of the energy is produced over the yearly cycle, but Figure 4-3 shows that is not the case. Taking into account the rated speed at 11.4 m/s, it is no surprise that the bins for 11 m/s and 12 m/s produce the most energy.

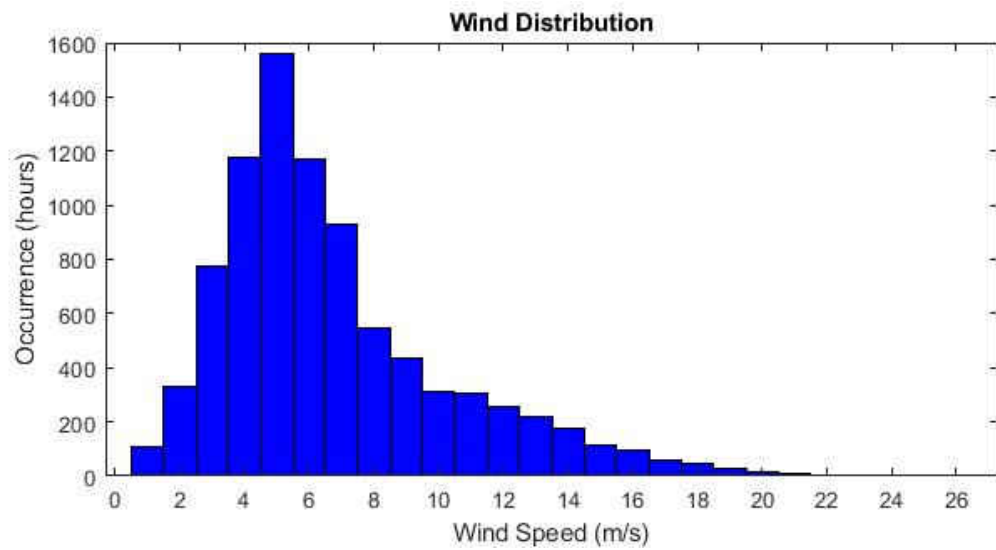


Figure 4-2. Wind Speed Distrubution

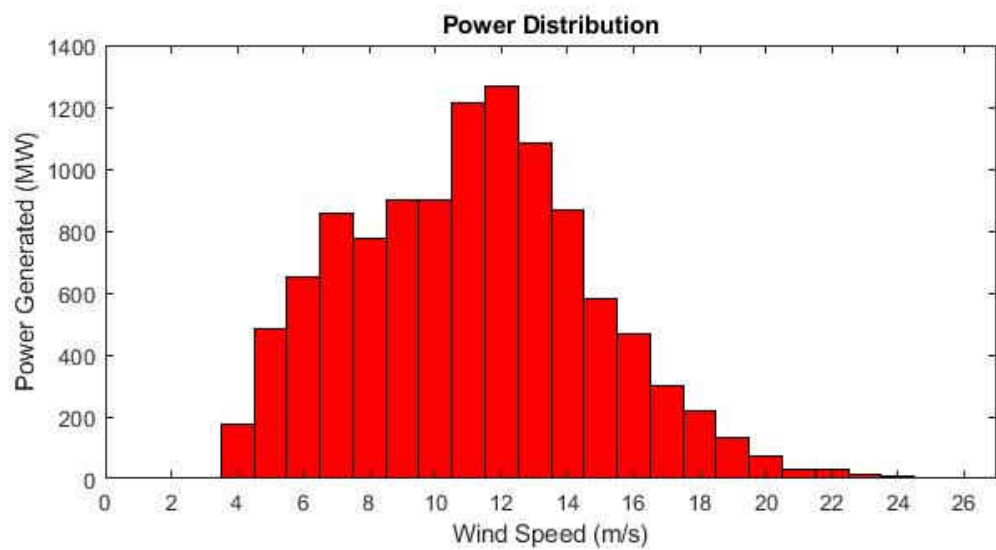


Figure 4-3. Estimated power generated distribution

Taking the sum of all the bins the estimated power that can be generated using Equation 2.1.1 is roughly around 11,000 MWh. This seems to match with the fact that the average onshore 3 MW turbine can produce around 6,000 MWh in a year [30]. It may be safe to assume

that the electricity produced will actually be greater than this estimate because of the fact the anemometer was not offshore where wind speeds are expected to be greater.

CHAPTER 5

RESULTS

SOWFA has 3 parts to it for simulating a wind plant. First step is to simulate an atmospheric boundary layer that is at least 3x3x1 km in the x,y and z directions respectively. The second step is to use or modify the NREL turbine simulation in SOWFA. For these simulations the original turbine was used. The next step is to use the data created from the precursor as the inflow for the intended turbine. This will put a turbine in an assigned location in the 3-D domain.

5.1 Precursor

The first step in creating a turbine simulation was to simulate a precursor simulation. The values created from this will later be used as inflow values for the wind plant simulations. Figure 5-1 shows visual representation of the wind profile in the z-direction (up). As can be seen from the figure, the wind speed increases as elevation increases.

Figure 5-1 Contours of velocity magnitude of simulated ABL represents an input wind velocity of 5.2 m/s at an elevations of 29.7 m high. For this simulation, the aerodynamic roughness height of the surface (z_0) is given a value of 0.0002 in the ABL conditions. This is the suggested value of z_0 for open water. The value for z_0 increases as surface roughness increases. For example, a value of 0.1 is generally used to simulate surfaces that has many trees and hedges. Mentioned in a previous section the surface roughness can increase in open water as

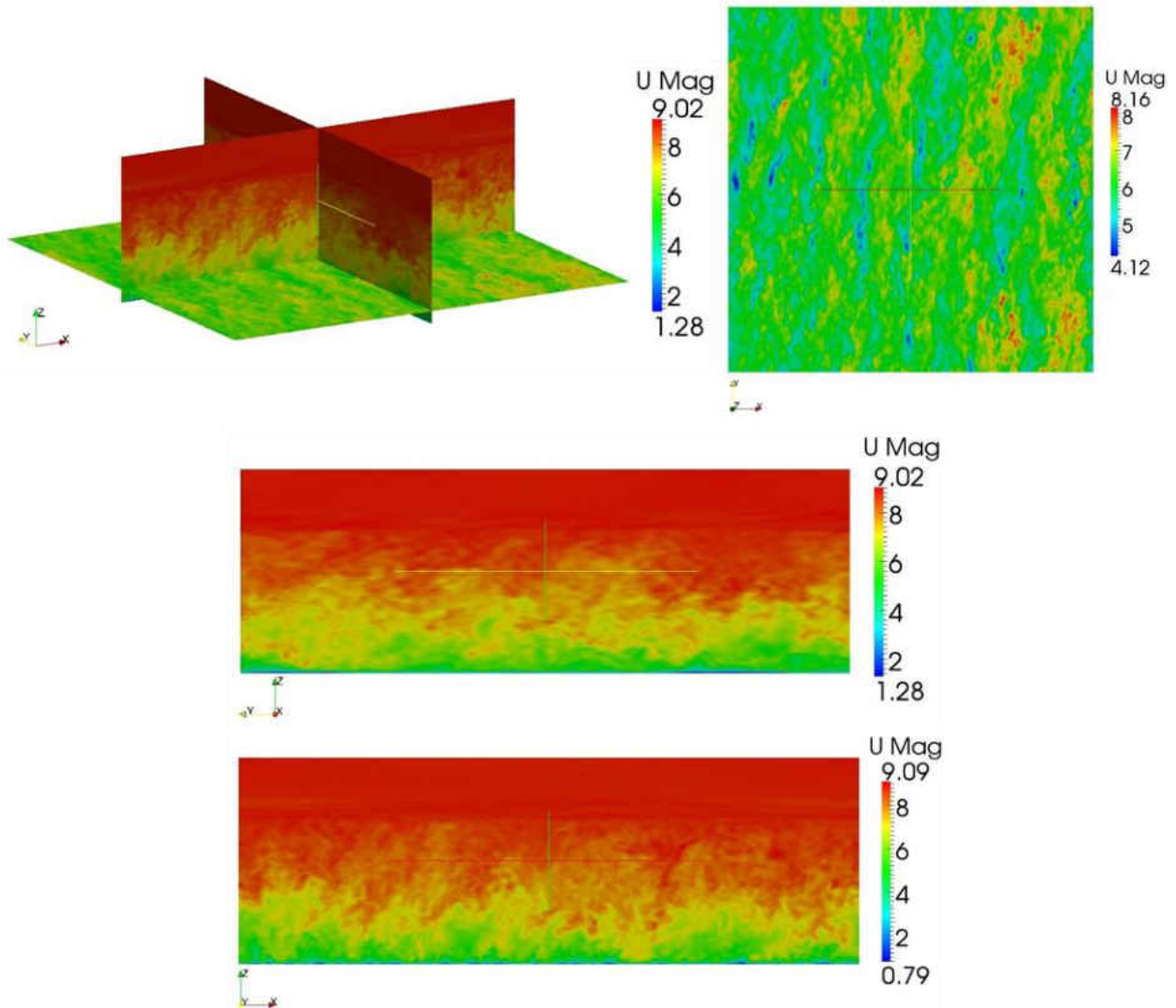


Figure 5-1 Contours of velocity magnitude of simulated ABL

a result of increased wind speed. The values for wind speed are 3.4 m/s (Figure 5-2), 5.2 m/s (Figure 5-3) and 9.6 m/s (Figure 5-4) all with the initial input elevation of 27.9 meters. As represented in the figures below, compare the time-averaged velocity along the z-axis. The simulations are compared to the Power Law

$$U_{z2} = U_{z1} \left(\frac{z_2}{z_1} \right)^\alpha$$

and the log wind profile

$$U_{z2} = U_{z1} \frac{\ln\left(\frac{z_2}{z_0}\right)}{\ln\left(\frac{z_1}{z_0}\right)}$$

U_{z1} is the velocity at the reference height (z_1) of 27.9 m. U_{z2} is the height to be calculated at height z_2 . α is the wind shear exponent with a value of 0.14 and z_0 is the roughness height with a value of 0.0002. This shows the results are similar to expectations. The sharp velocity increase around the 700 m position can be explained when compared to the temperature profile.

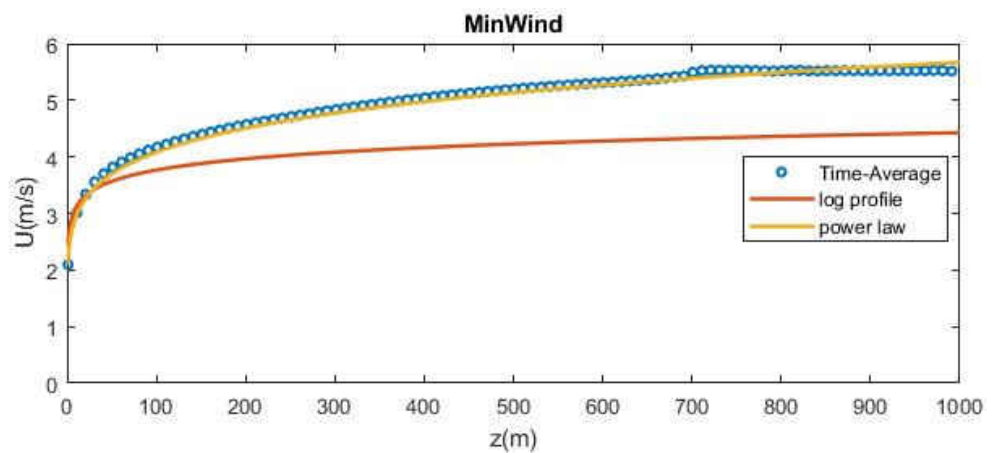


Figure 5-2. Time-averaged simulated velocity vs elevation z for 3.4m/s

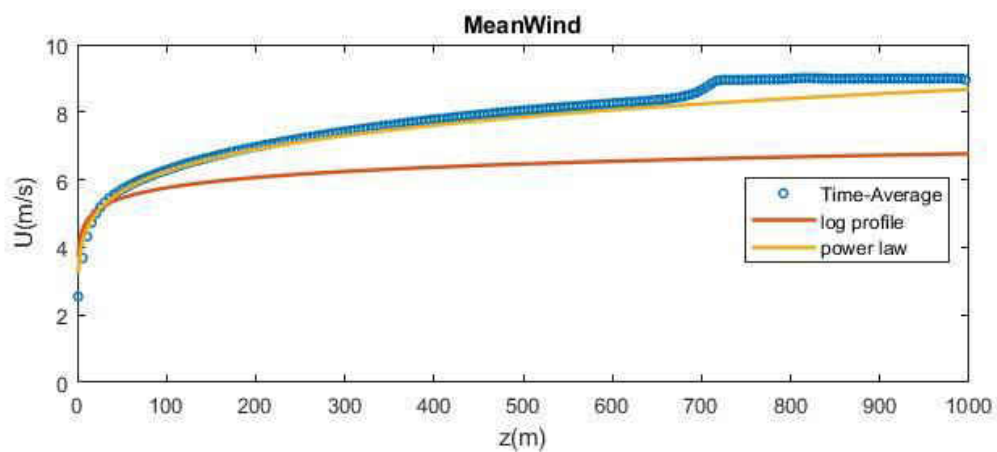


Figure 5-3. Time-averaged simulated velocity vs elevation z for 5.2m/s

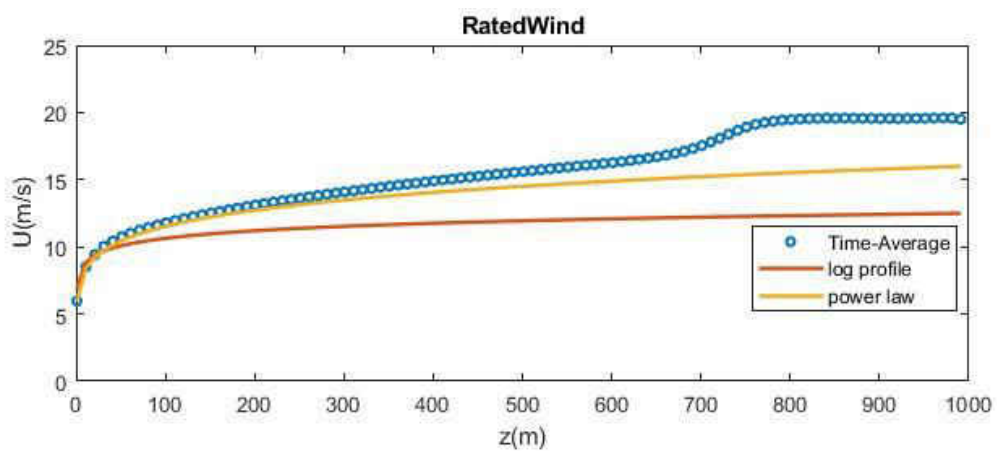


Figure 5-4. Time-averaged simulated velocity vs elevation z for 9.6m/s

The sudden increase of temperature is due to a defined capping inversion. This slows down the boundary layer vertical growth. Temperature is kept at a constant value up to a certain height before it starts to increase. In these cases, it was set around 700 m in elevation. The constant temperature for Figure 5-6 is set to a different value than the temperatures for Figure 5-5 and Figure 5-7. This also shows that a minor change of temperature does not affect the temperature profile in these simulations and that the wind speed does not greatly affect the temperature profile either.

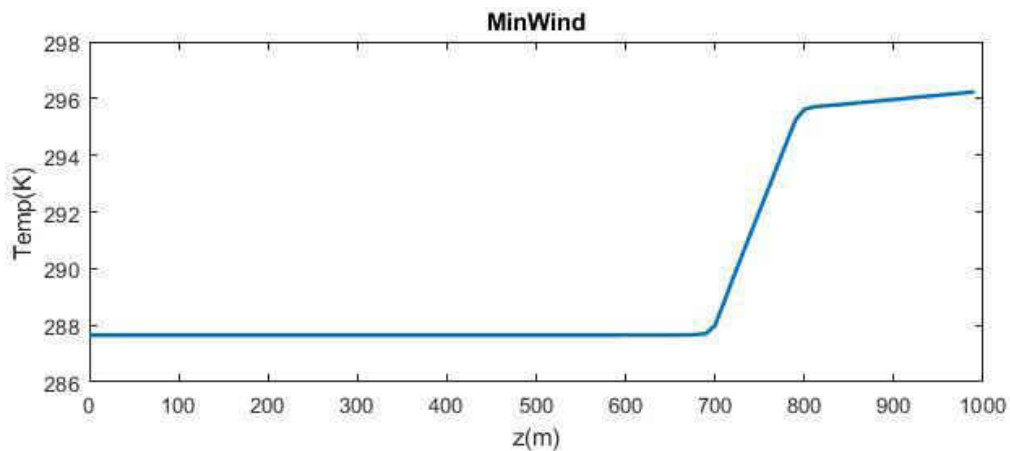


Figure 5-5. Mean temperature for simulation using 3.4m/s as initial velocity

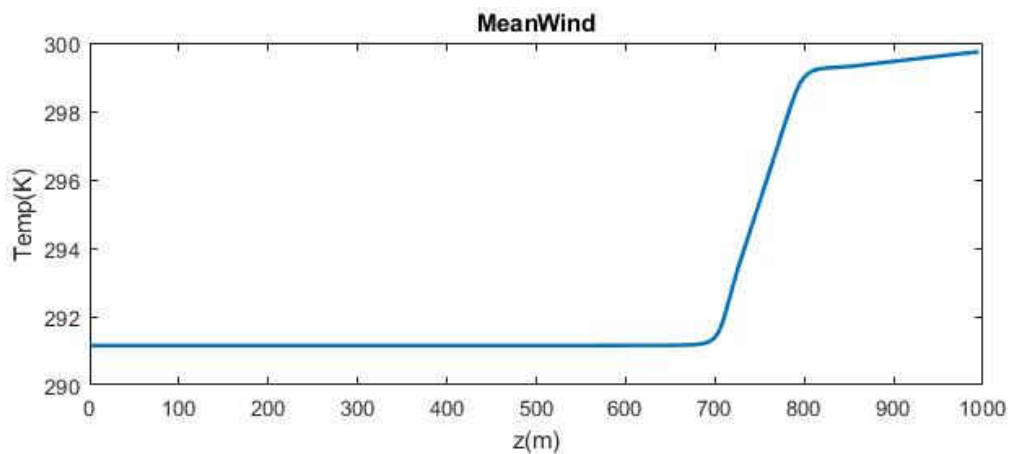


Figure 5-6. Mean temperature for simulation using 5.2m/s as initial velocity

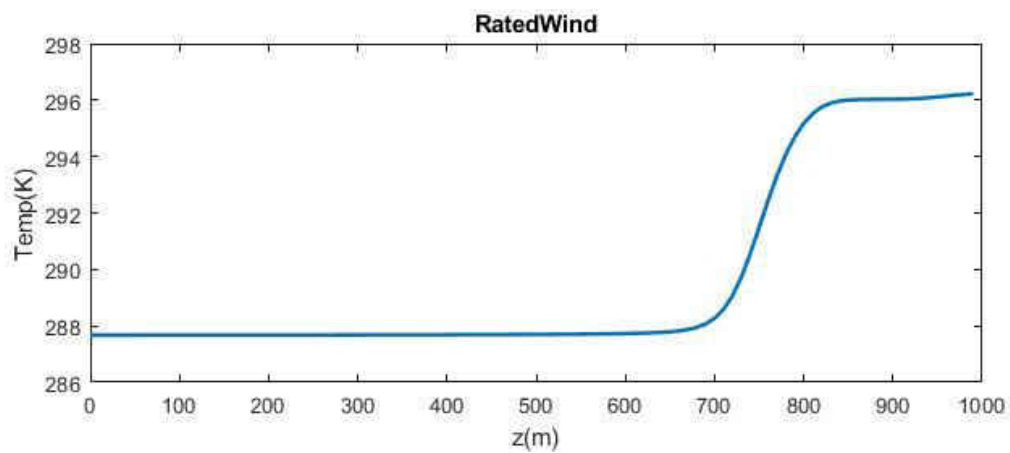


Figure 5-7. Mean temperature for simulation using 9.6m/s as initial velocity

5.2 Turbine Simulations

The turbine simulation starts off with a constant velocity for inflow. Three separate simulations were performed; in these cases, the value is taken from using the precursor simulations average value at around 90 meters in elevation. For example, the precursor with an inflow velocity of 5.4 m/s at 27.9 m in elevation had an average wind velocity of 6.2 m/s at around 90 m in elevation. Using this method, the inflow velocities were 4.1 m/s, 6.2 m/s and 11.6 m/s, respectively.

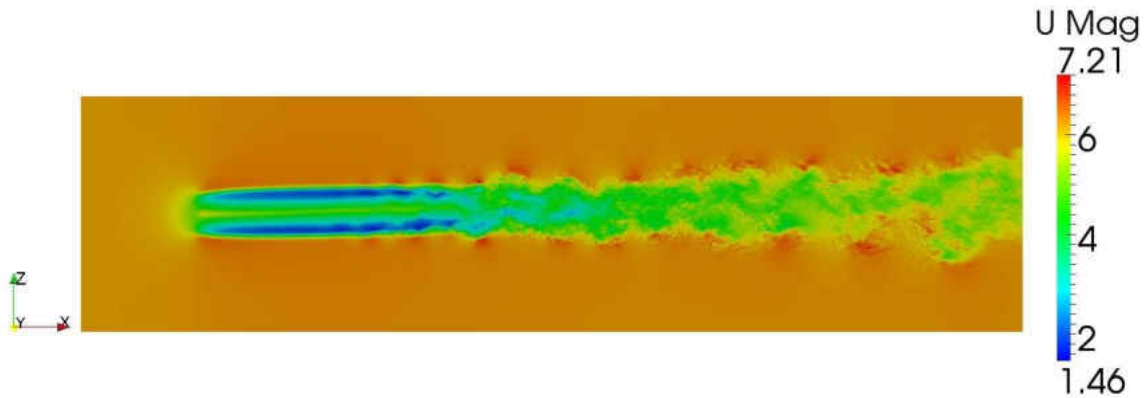


Figure 5-8 Contours of velocity magnitude at t=12000 seconds

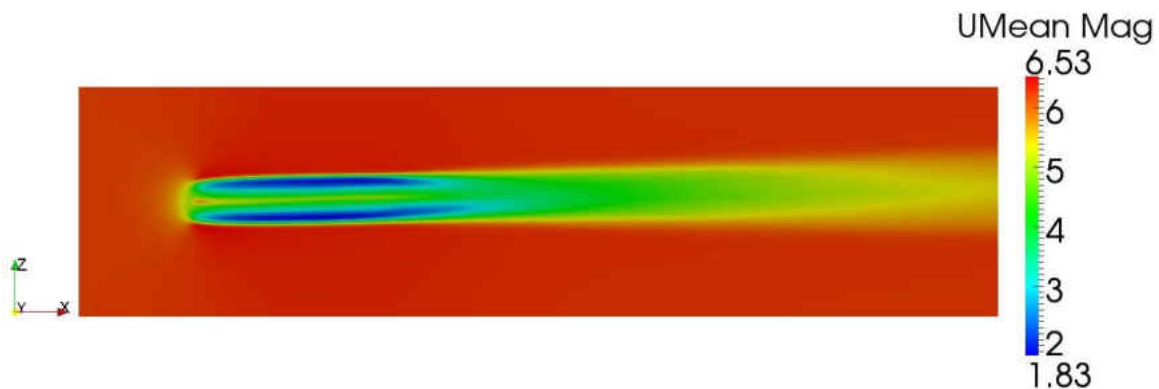


Figure 5-9 Contours of the time-averaged velocity magnitude

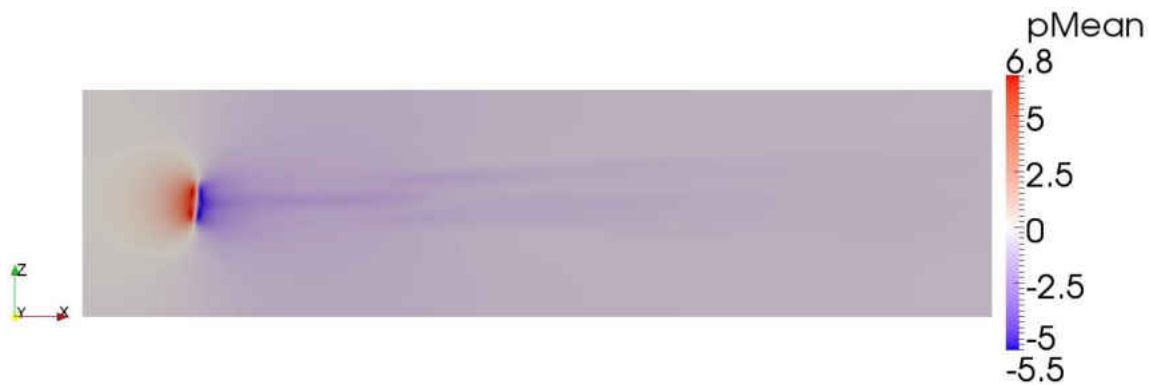


Figure 5-10 Contours of pressure averaged over time

Figure 5-8 Contours of velocity magnitude at $t=12000$ seconds, Figure 5-9, and Figure 5-10 are the SOWFA contours of the turbine simulation at velocity of 6.2 m/s. Figure 5-8 shows the velocity at the time step of 1800 seconds, while Figure 5-9 shows the mean velocity and shows a more distinct stream tube behind the turbine. Also, as discussed previously, it shows that the velocity in front of the turbine also goes through a decrease in wind speed. Figure 5-10 shows that the pressure increases as it approaches the blades then starts from a negative value immediately behind the blade and starts to increase as it flows downstream. These confirm some of the expected results as shown previously in Figure 3-1, and would look similar for the other 2 cases. In order to get a better understanding, it would be worth looking into the extracted values at the blade.

To smooth out the blade data obtained from the turbine simulation, averaging the data over time or a spatial location would give a better idea how the calculated blade values change as it rotates along the axis. Figure 5-11, shows the azimuth blade angle in respect to origin over time. In this figure the dotted line does not represent any values but shows that the azimuth at 0 degrees and 360 degrees are the same position along its rotation.

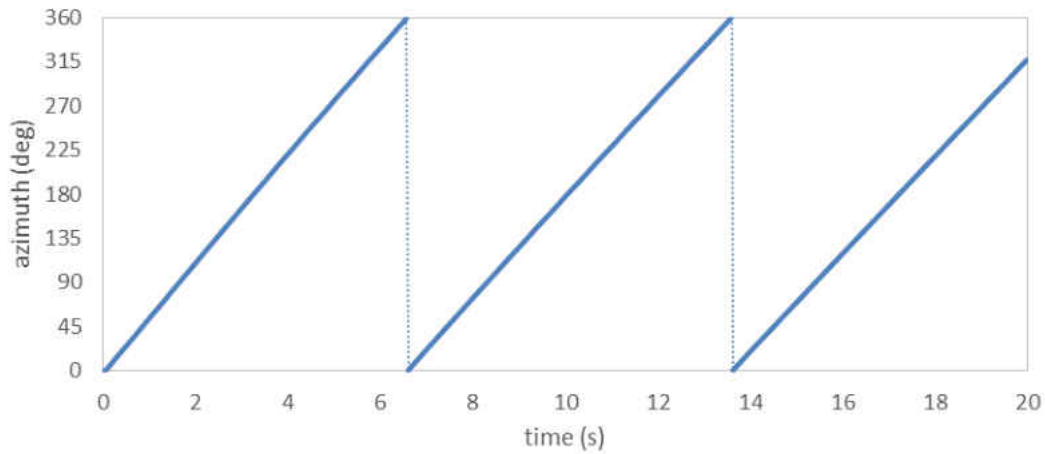


Figure 5-11 Azimuth for 6.2 m/s inflow

The first set of figures (Figure 5-14, Figure 5-16, Figure 5-19, Figure 5-21, Figure 5-24, Figure 5-26, Figure 5-28, Figure 5-30, Figure 5-32, and Figure 5-34) for each data category plots the average value of each point along the blade. These plots only review the data compiled along 1 of the 3 blades as the other blades will give similar results. For these data points along the blade, there is a dotted line connecting each point; this dotted line does not have any significance. The second set of the figures (Figure 5-15, Figure 5-17, Figure 5-20, Figure 5-22, Figure 5-25, Figure 5-27, Figure 5-29, Figure 5-31, Figure 5-33, and Figure 5-35) for each section makes use of averaging the blade by its position along its axis (or azimuth) and only looks at the results at the tip of the blade at 63 meter from the center. The results were grouped by degrees of 1, meaning there is a group for 1 to 360. When the azimuth is at 0 or 360 this means that the blade is pointing straight up as seen in Figure 5-12.

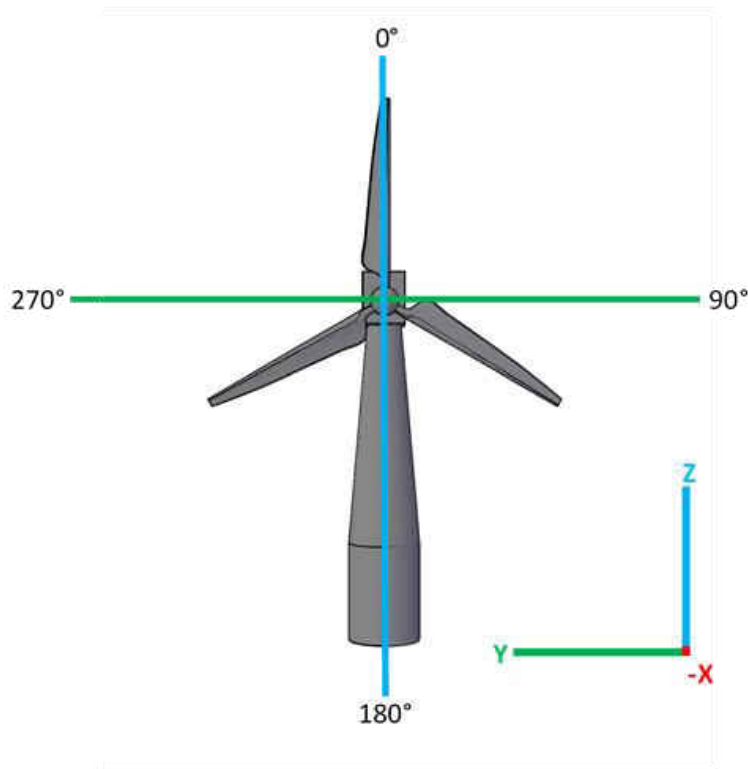


Figure 5-12. Azimuth positions

5.2.1 Axial Velocity

Figure 5-13 shows that the axial flow is perpendicular to the turbines plane and flows in the X direction for these simulations. In order to calculate the force on each blade point, the inflow wind velocity must be determined. As discussed in the momentum theory, the velocity will decrease before it reaches the blade, which the plots show since there is no point along the blade where the velocity is greater than the inflow wind speed. In Figure 5-14, the computed axial velocity along the blade is the greatest near the center of the turbine and starts to decrease along the blade in the center then starts to increase towards the tips of the blade. There also appears to be a trend of the higher wind speeds to have an axial velocity that decreases/increases more and at a quicker rate towards the hub and tip of the blades.

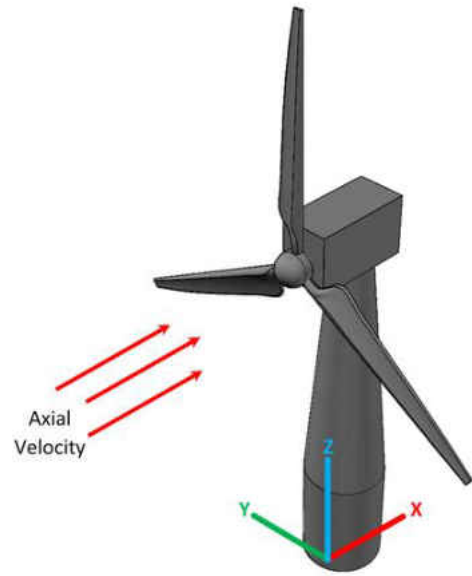


Figure 5-13. Direction of axial velocity in relation to the turbine

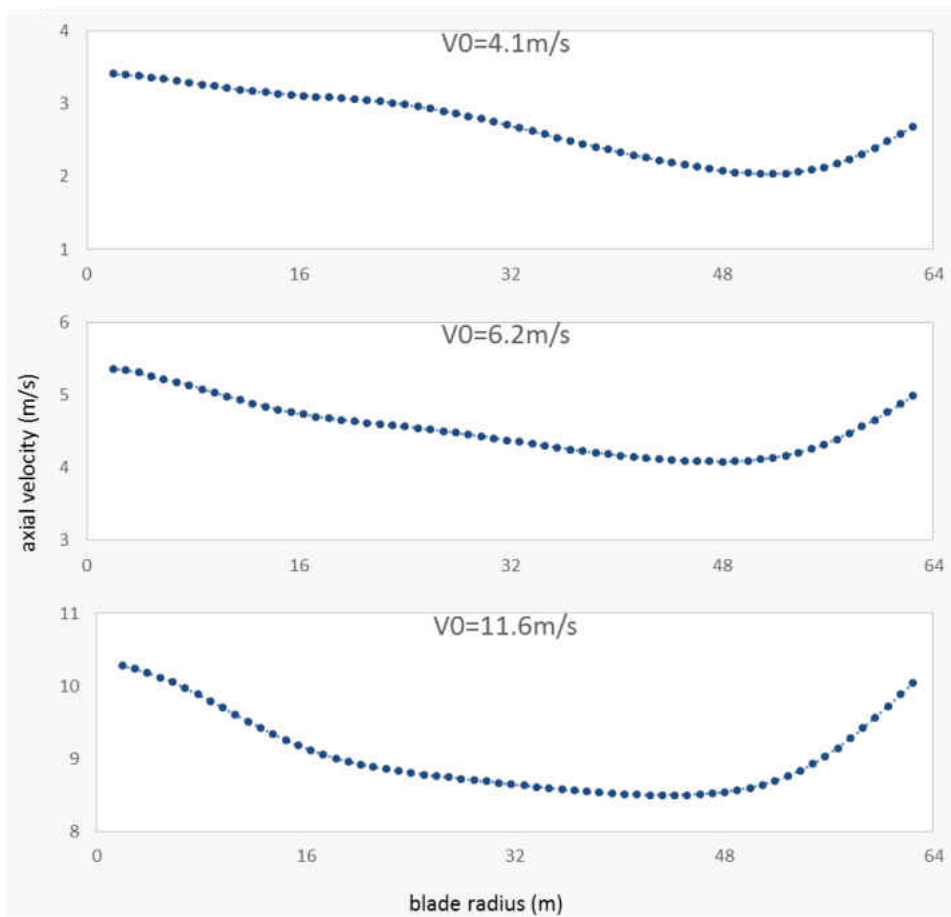


Figure 5-14. Computed averaged axial velocity along blade

The values for axial velocity change depending on their position along the axis. Figure 5-15 represents the data along the turbines tip and suggest that the axial velocity is greatest when its angle is around 180 degrees if inflow is uniform and constant.

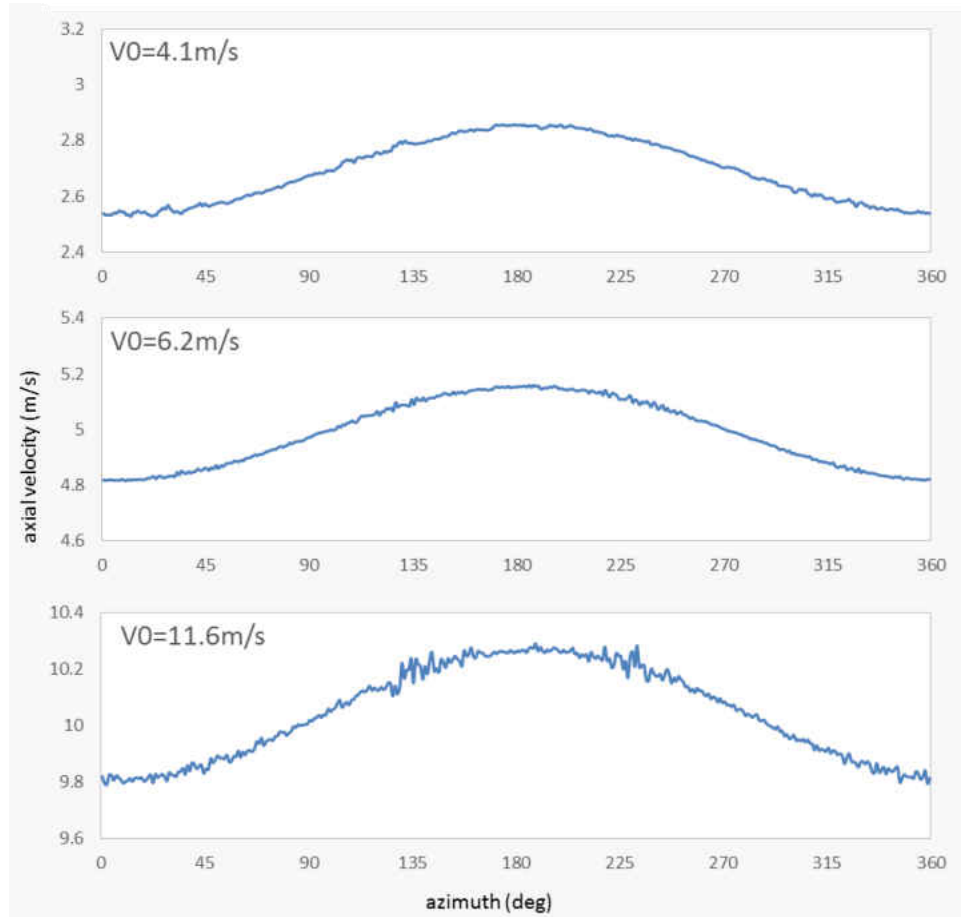


Figure 5-15. Computed axial velocity of blade tip averaged along azimuth

5.2.2 Tangential Velocity

The next data to look at is the tangential velocity (Figure 5-16), which in these SOWFA results refers to $(\Omega r - V_\theta)$ in Equation 3.2.6. The rotation rate of the turbine depend on the inflow velocity, which directly influences the tangential velocity. The results show a linear increase with Ωr being the main contributing factor in the tangential velocity for these simulations. For example, at 6.2 m/s the blades rotate at 8 rpm which equals to around 52 m/s for tangential velocity which agree with the results.

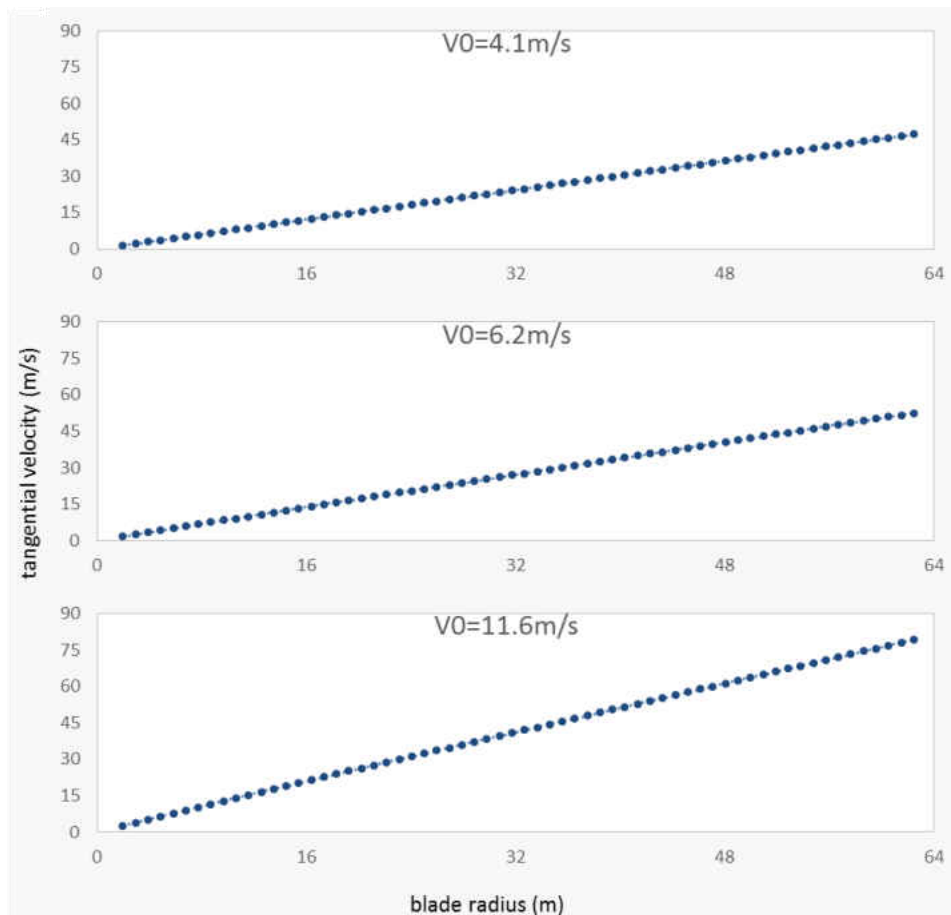


Figure 5-16. Computed average tangential velocity along blade

The tangential velocity cycle appears to be affected by the gravitational force in Figure 5-17. This can be seen from the fact the velocity is at its highest and lowest when parallel to the ground. At 90 (Figure 5-18.A) degrees the blade is moving in a downward direction parallel to the ground and at 270 (Figure 5-18.B) degrees the opposite is true.

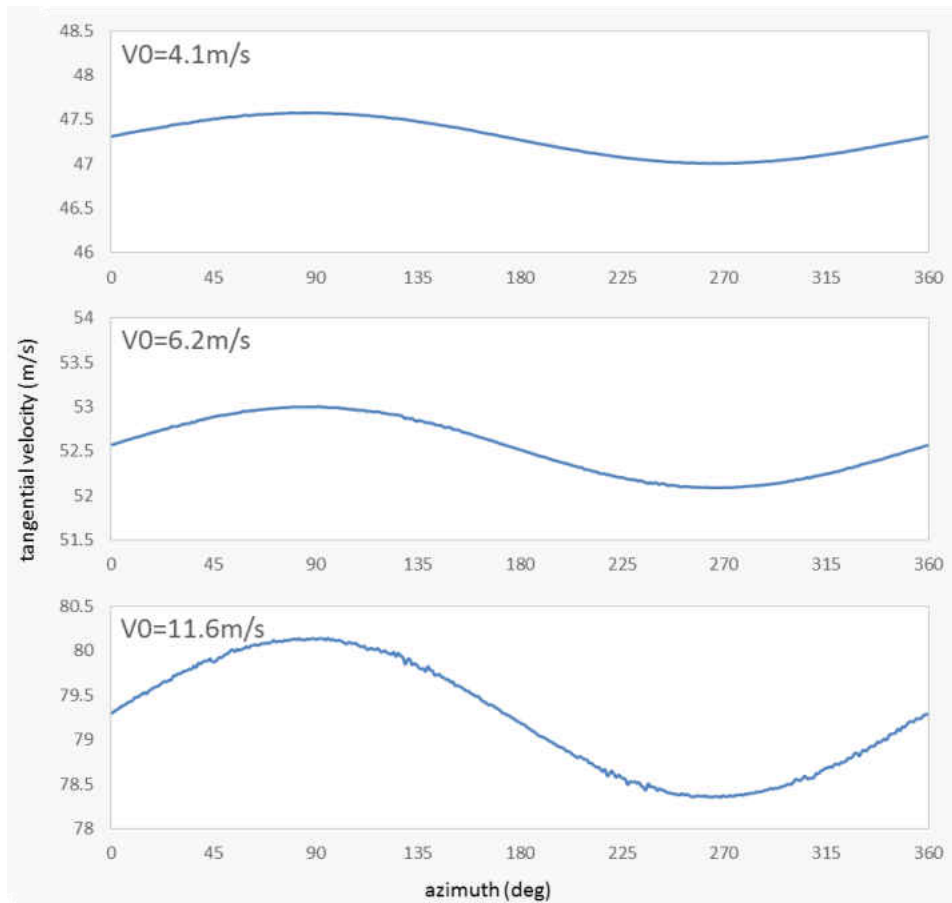


Figure 5-17. Computed tangential velocity of blade tip averaged along azimuth

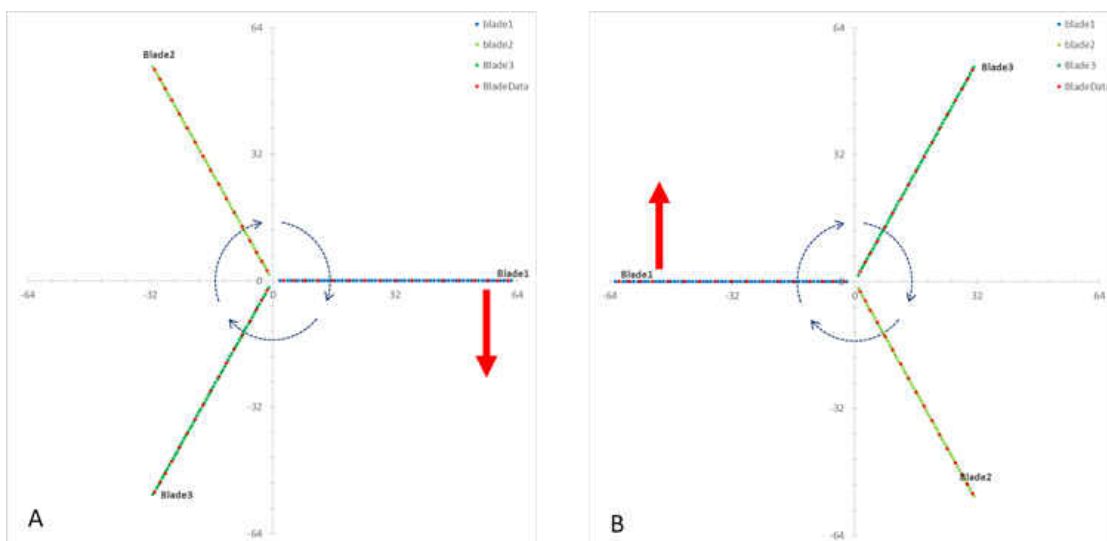


Figure 5-18. A) Blade position at 90° B) Blade position at 270°

5.2.3 Velocity Magnitude

Modifying Equation 3.2.6 to match the terms used in SOWFA, the equation becomes

$V_{mag} = \sqrt{V_x^2 + (\Omega r - V_\theta)^2}$. With this SOWFA output results can be calculated and confirmed in Figure 5-19. As expected the tangential velocity contributes more to the velocity magnitude, especially closer it gets to the tips.

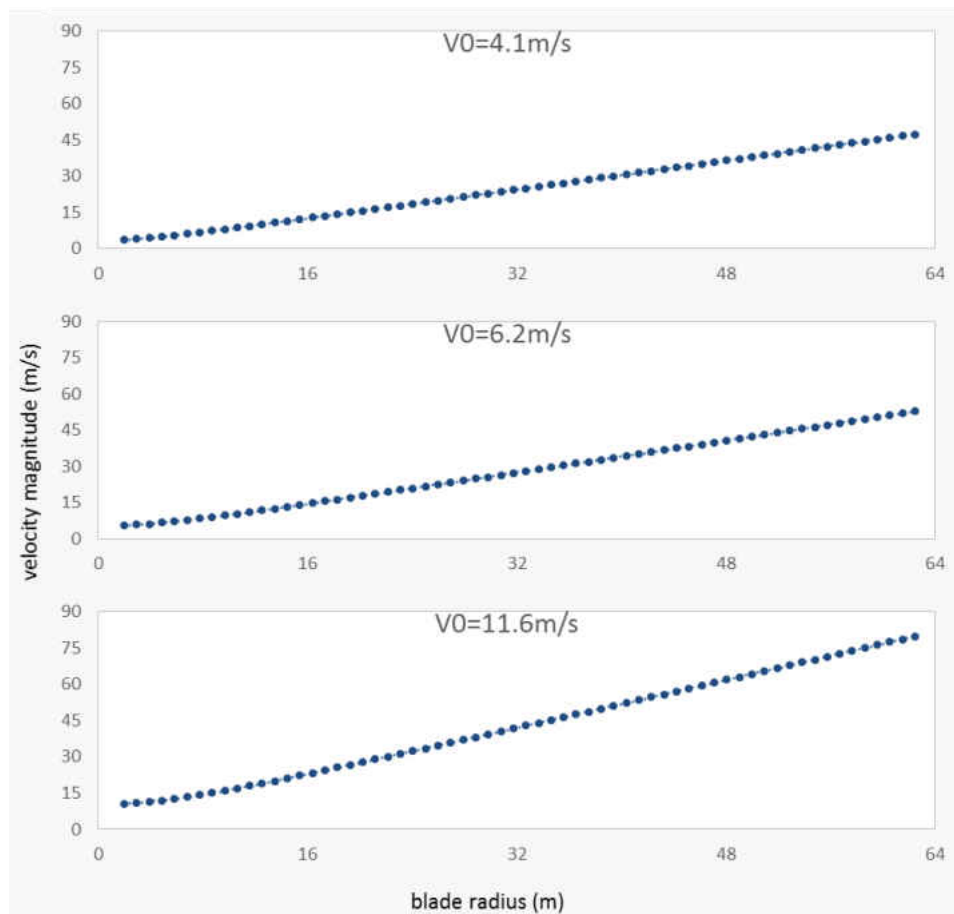


Figure 5-19. Computed average velocity magnitude along blade

In Figure 5-20, the tangential velocity is the greater contributor to the magnitude. For example, at $V_0 = 11.6$ m/s, axial velocity at the tip is around 10 m/s, while the tangential velocity is around 80 m/s.

$$V_{mag} = \sqrt{10^2 + (80)^2} = 80.6 \text{ m/s.}$$

It should be expected that Figure 5-20 will have a very similar pattern and values as the tangential velocity near the tip of the blade (Figure 5-17) where tangential velocity is at its greatest.

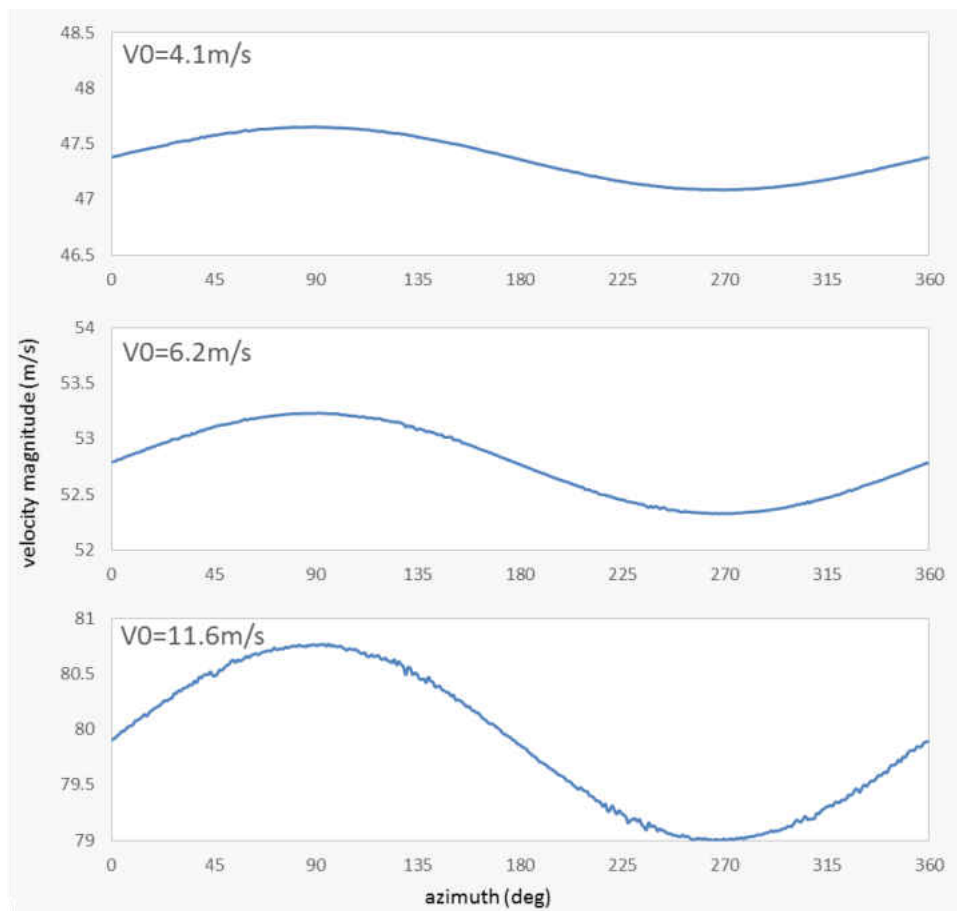


Figure 5-20. Computed velocity magnitude of blade tip averaged along azimuth

5.2.4 Alpha

With axial velocity and tangential velocity, the angle of attack (α) can be determined. Solving alpha is necessary to determine the coefficient of lift and coefficient of drag seen in equations 3.2.9 and equation 3.2.10. To solve for the alpha the equations 3.2.7

$$\alpha = \varphi - \gamma$$

and equation 3.2.8 are used.

$$\varphi = \tan^{-1} \frac{V_x}{\Omega r - V_\theta}$$

In equation 3.2.7, γ is the local pitch angle which is equal to twist angles in table 3-2 for these simulations. The turbine will start to turn the blade to increase the pitch angle when the wind speed is greater than the rated wind speed in order to keep an ideal tip speed ratio. If the twist angle (γ) is greater than the flow angle (φ) then alpha can be negative as seen in the result for $V_0 = 3.4$ m/s.

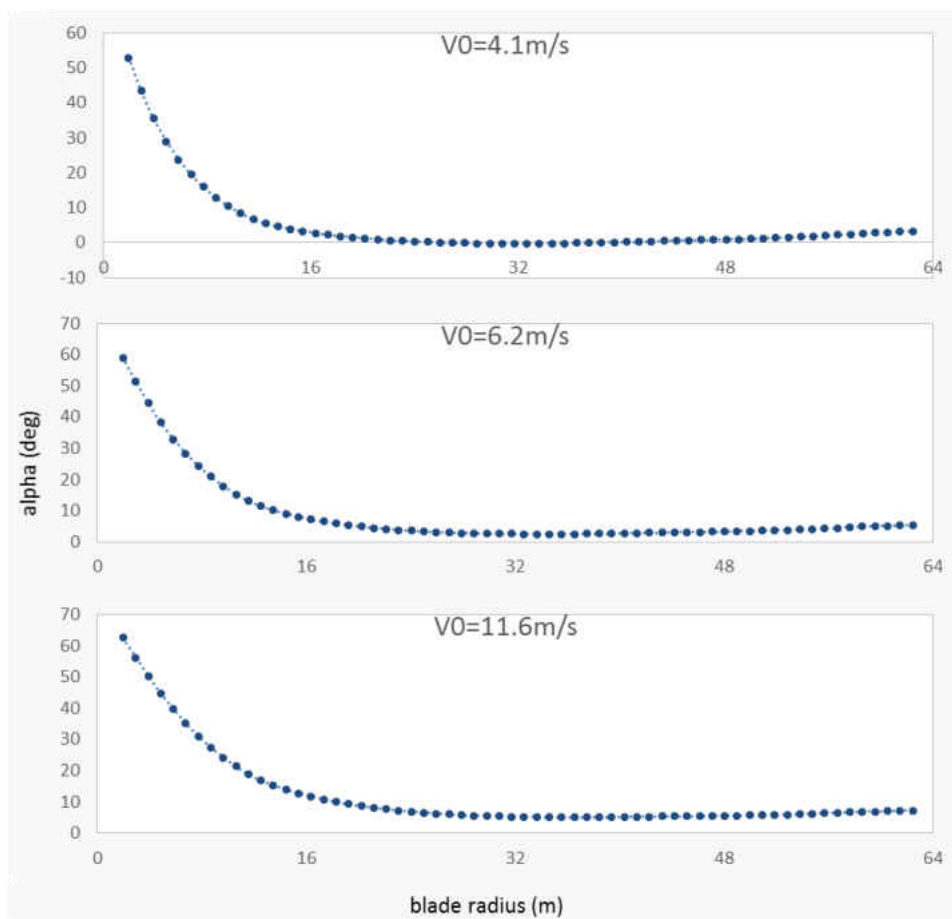


Figure 5-21. Computed averaged alpha along blade

Using equation 3.2.7 and equation 3.2.8 the results from SOWFA can be checked to see if the results are the expected values for the alpha. The blue line in Figure 5-22. Computed alpha of blade tip averaged along azimuth represents the results, while the red represents the estimated values for alpha using the equations. Alpha is necessary in determining the coefficients of lift and drag in the airfoils tables in Appendix A. The differences will come from the small fluctuations of V_θ , where its effects become less as the blade rotation speed increases.

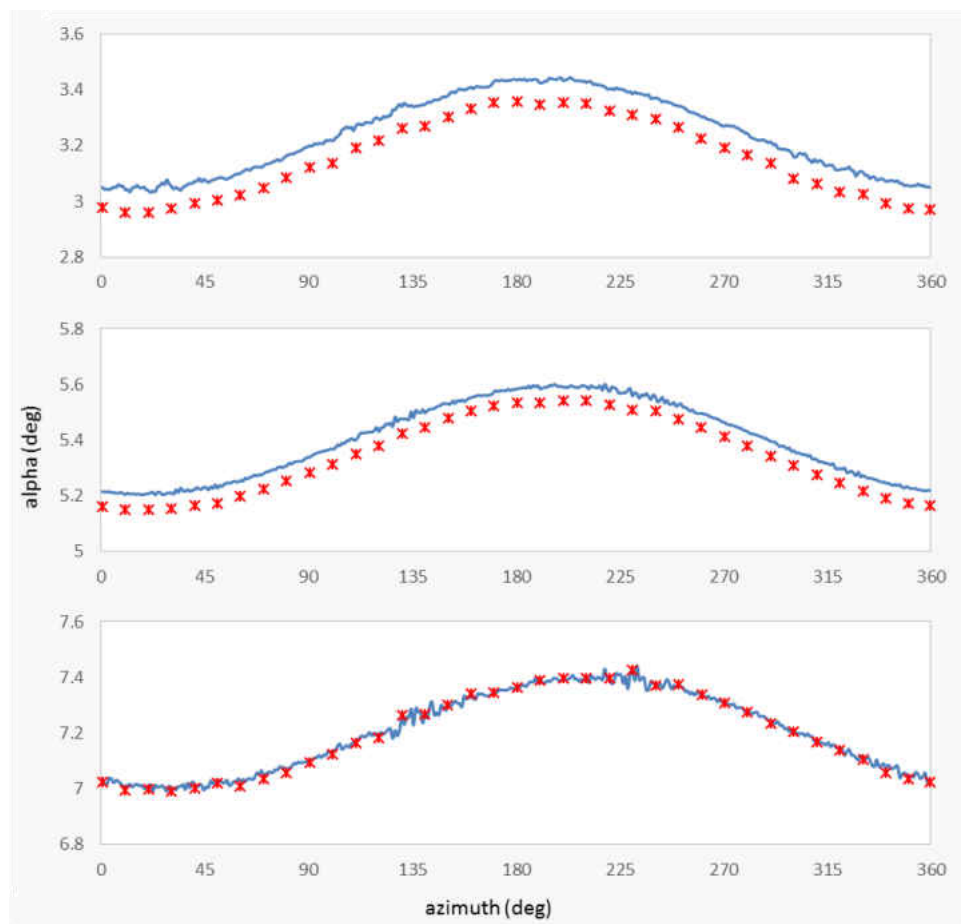


Figure 5-22. Computed alpha of blade tip averaged along azimuth

5.2.5 Coefficient of Drag

Once α has been calculated, the drag and lift coefficient can be determined. C_d and C_l values depend directly on the values of α , by using the airfoil properties in Appendix A. For example, NACA64 is used near the tip of the blade. In NACA64, when α is 5 degrees would have a C_d of 0.0058 and a C_l of 1.011. Also notice in Figure 5-24 that the first nine data points along the blade are constant across each test case. This is because C_d is 0.5 for the airfoil Cylinder1 and 0.35 for the airfoil Cylinder2 which correspond to those points. Figure 5-23 gives a visual understanding of why Cylinder1 and Cylinder2 have constant values.

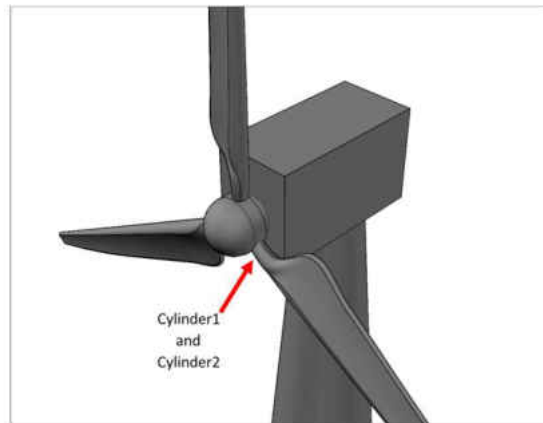


Figure 5-23. Cylinder1 and Cylinder2 reference point

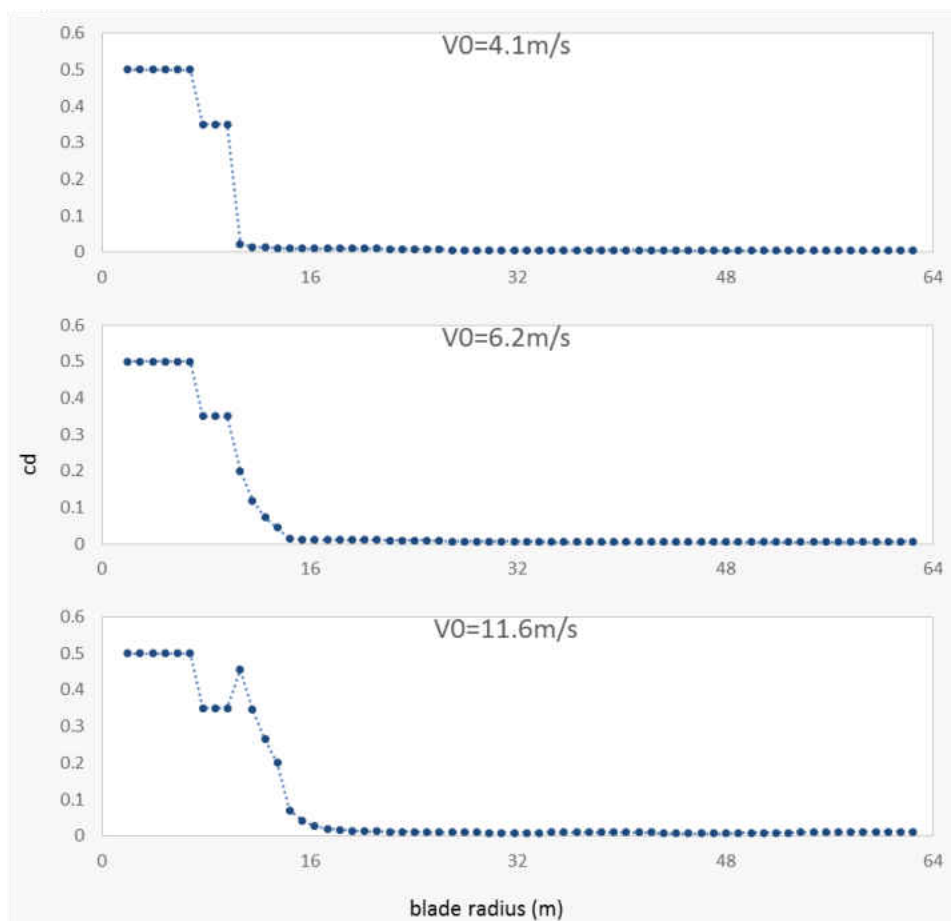


Figure 5-24. Computed averaged C_d along blade

Figure 5-25 references NACA64 in Appendix A to determine the coefficient of drag. This airfoil shows that drag will get to be very small the closer alpha gets to 0.

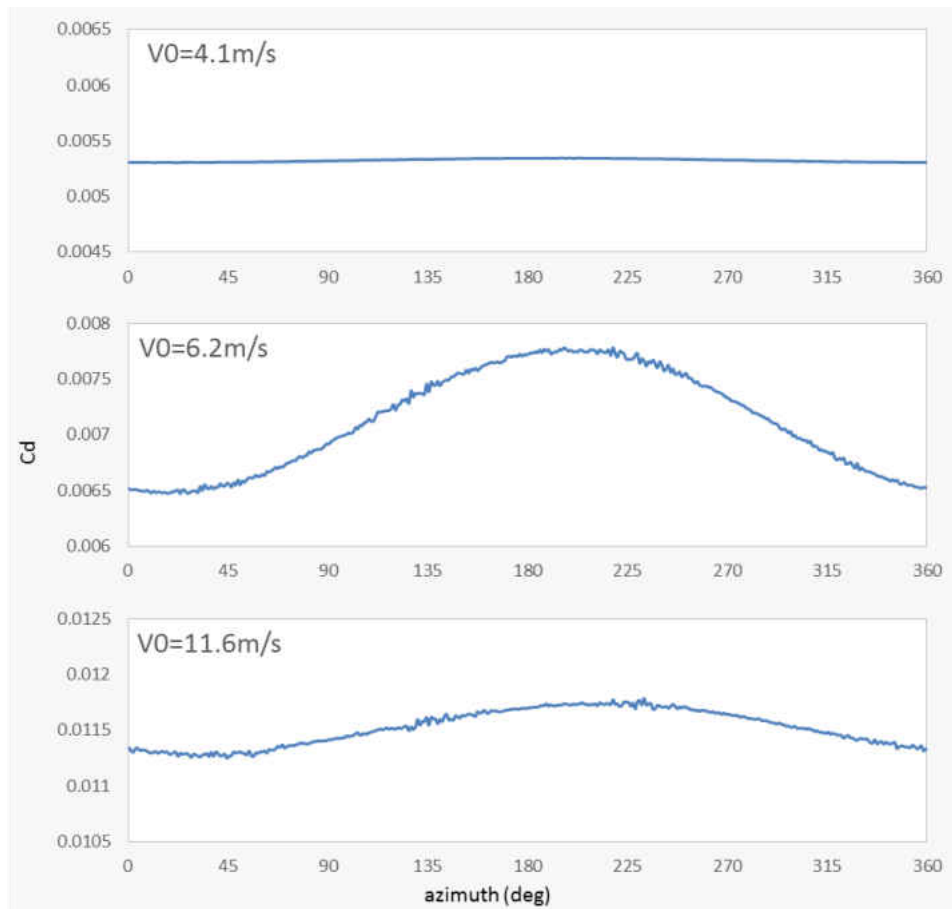


Figure 5-25. Computed C_d of blade tip averaged along azimuth

5.2.6 Coefficient of Lift

Again the first nine data points are constant across all three results, but this time the values are 0 for the points that reference Cylinder1 and Cylinder2 in Figure 5-26. The value for the coefficient of lift is 0 because this is the cylinder section connected to the blade. You may have noticed that in previous plot and this one that the points group into distinct sections. This is due to the fact that each section is referencing a different airfoil.

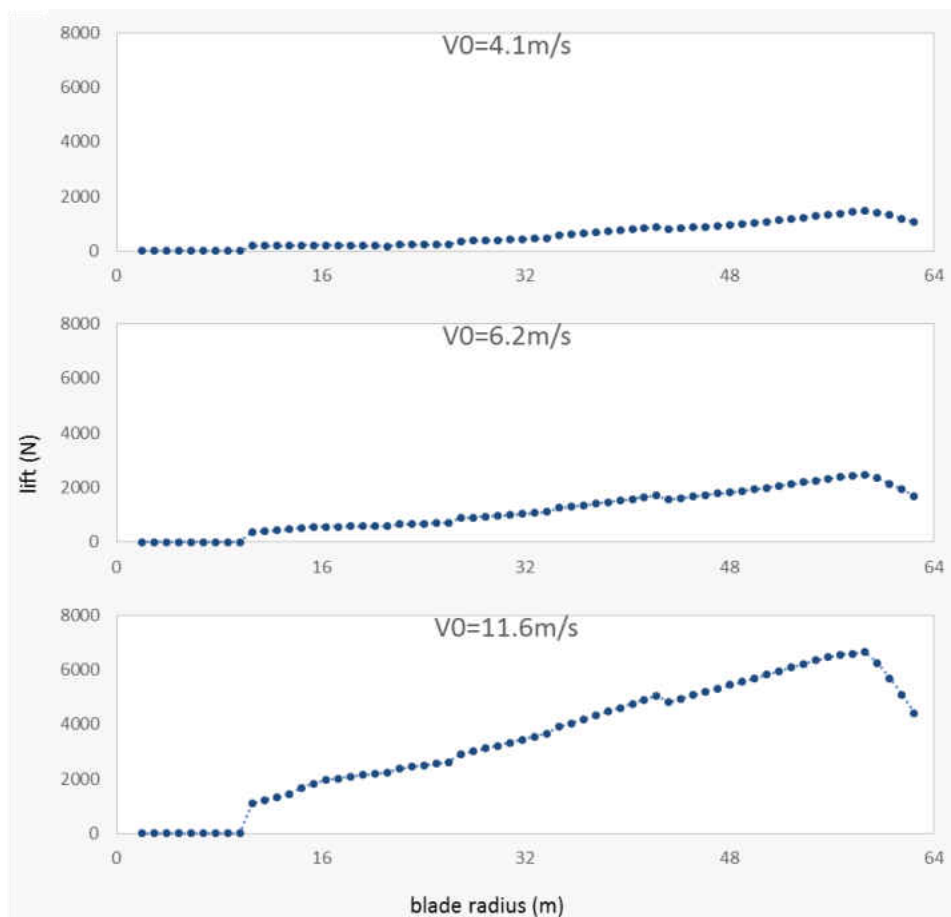


Figure 5-26. Computed averaged CI along blade

Figure 5-27 shows the coefficient of lift's fluctuation along the azimuth and gives a closer look at its values that correspond to alpha in Figure 5-22.

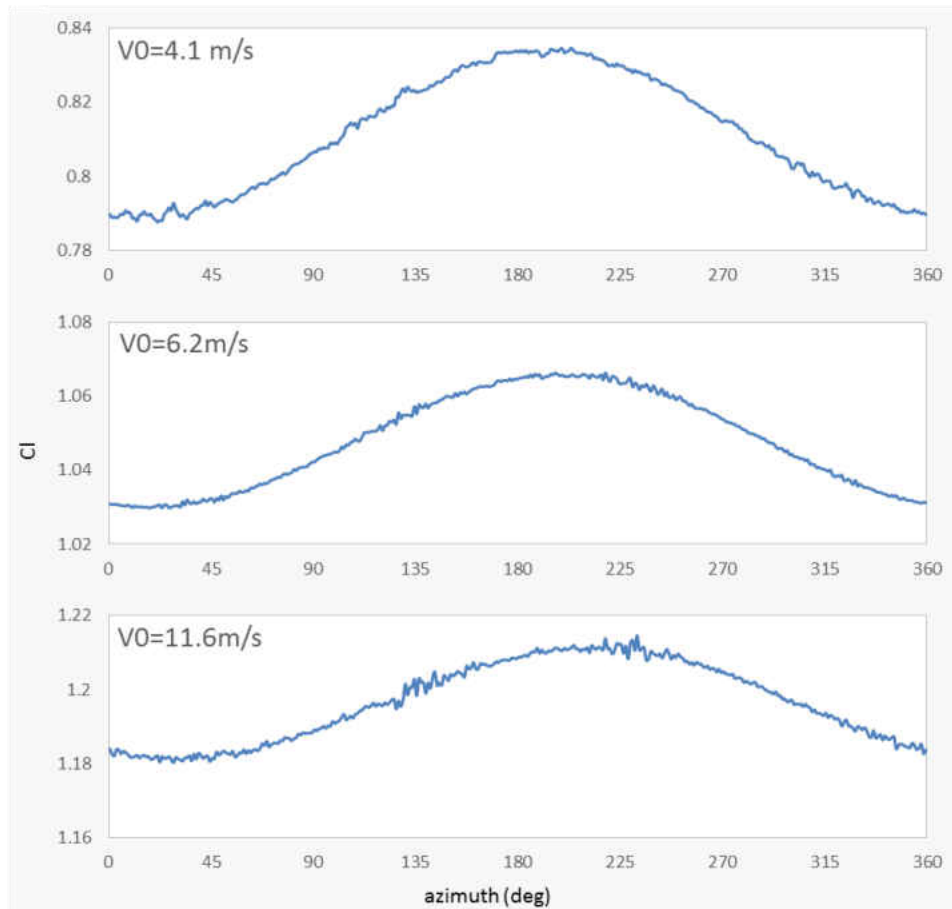


Figure 5-27. Computed C_l of blade tip averaged along azimuth

5.2.7 Drag

Now that the coefficient of drag is available, Equation 3.3.10 can be used to confirm the values for drag in Figure 5-28.

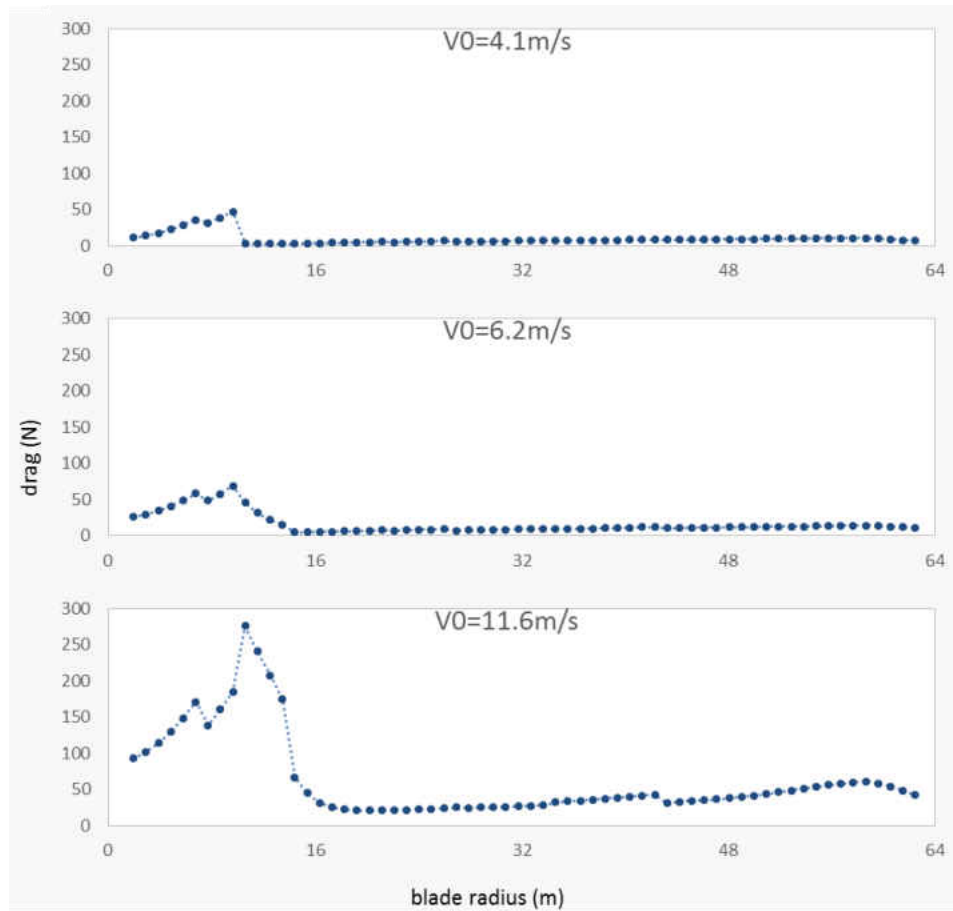


Figure 5-28. Computed average drag along blade

In Figure 5-29, it appears that drag does not have the same periodic fluctuations along the azimuth. This different periodic fluctuation is most likely due to the relationship between the different values of C_d and Velocity in Equation 3.2.10.

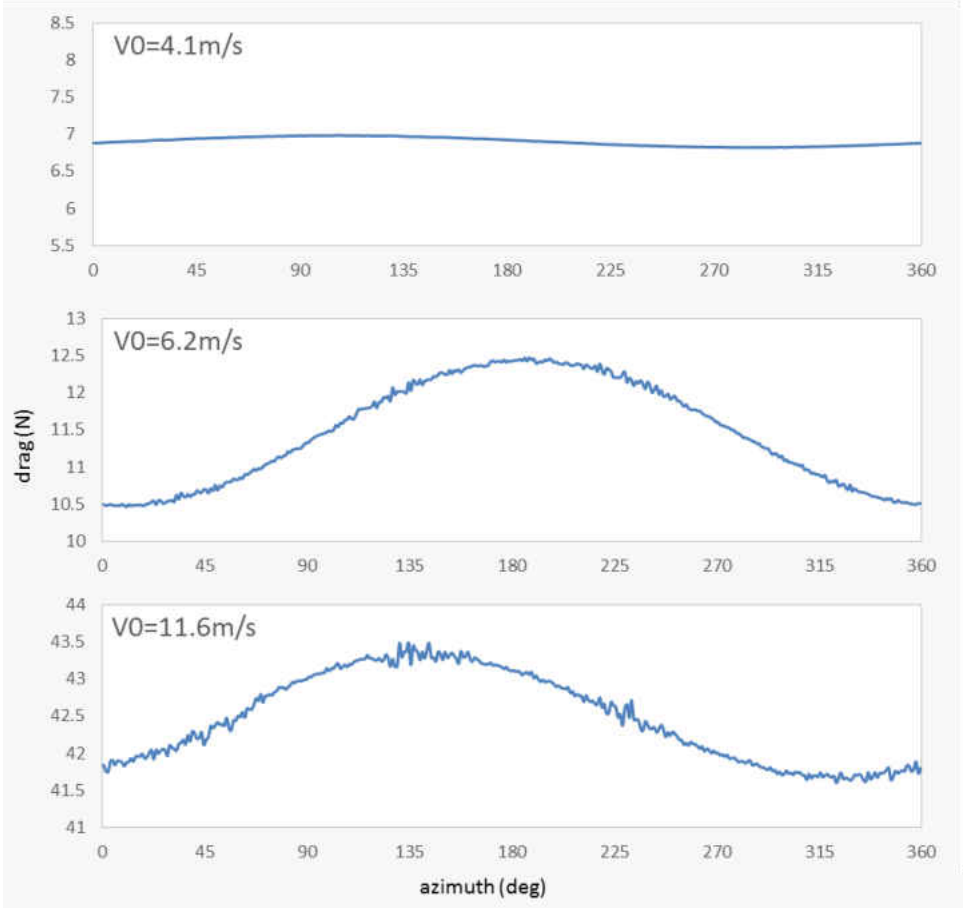


Figure 5-29. Computed drag of blade tip averaged along azimuth

5.2.8 Lift

As was the case for drag, lift (Figure 5-30) can be solved in a similar way using the coefficient of lift. Equation 3.2.9 would be the equation to reference when solving lift.

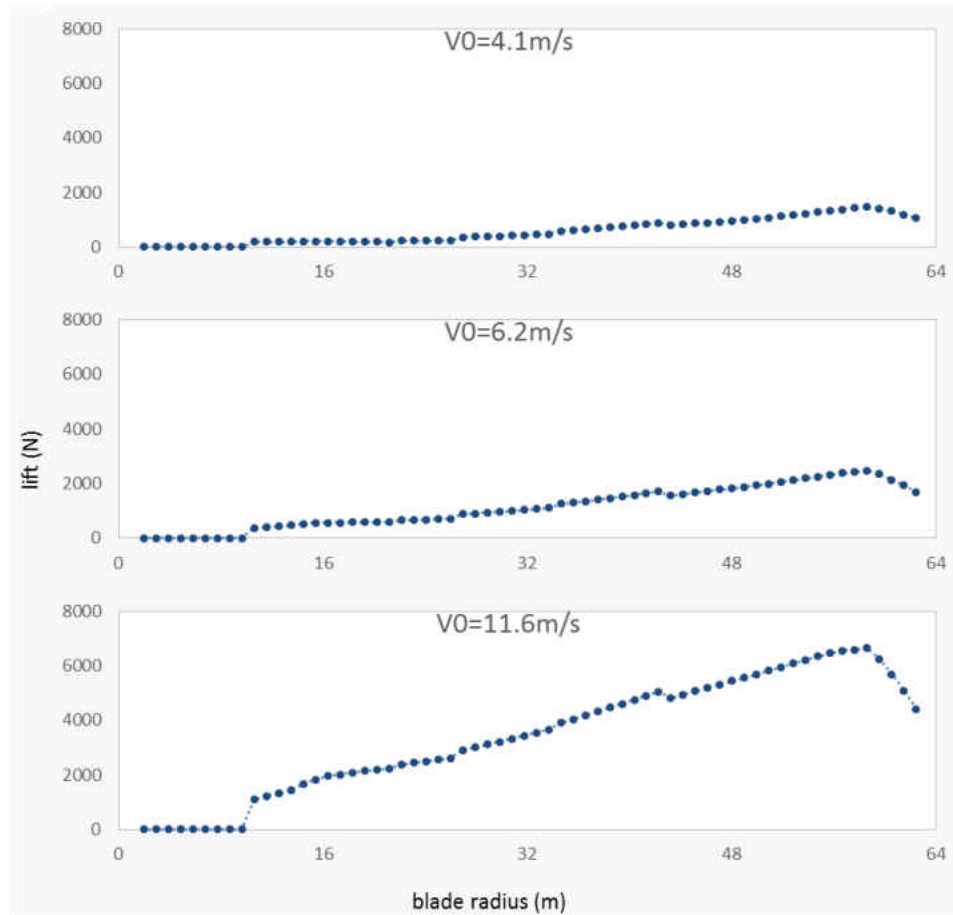


Figure 5-30. Computed averaged lift along blade

As was the case for drag, Figure 5-31 does not seem to have a constant periodic fluctuation between the three cases.

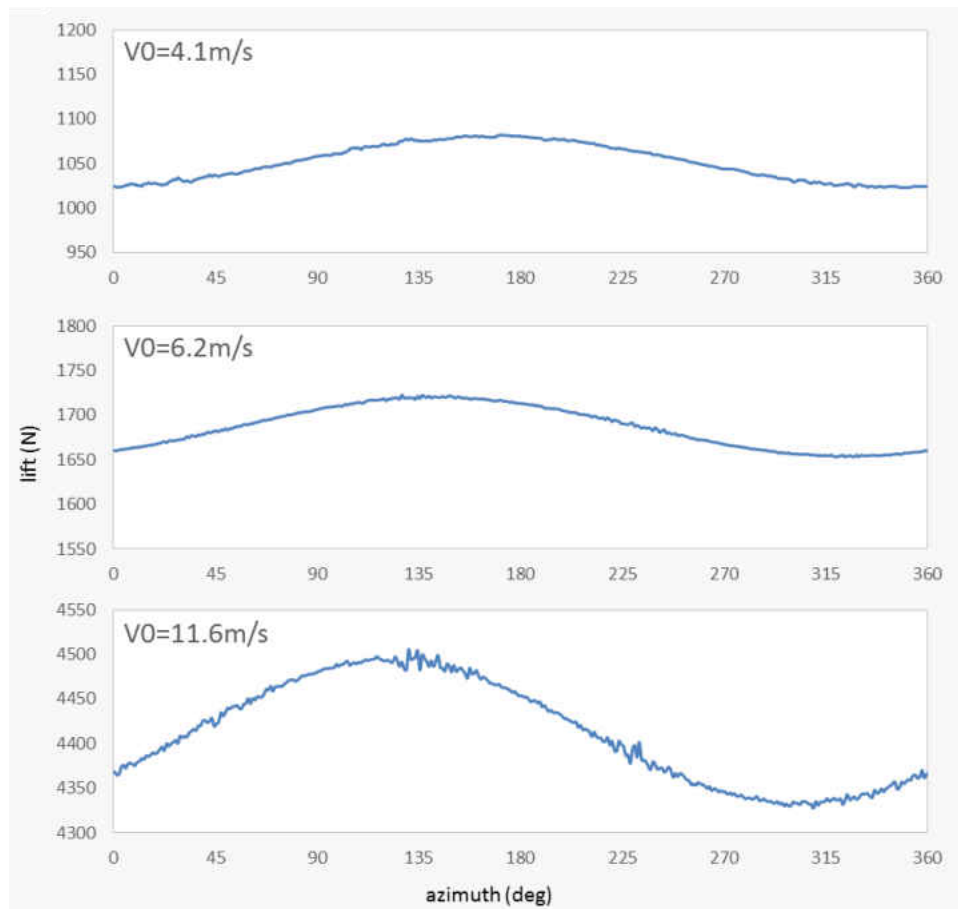


Figure 5-31. Computed lift of blade tip averaged along azimuth

5.2.9 Axial Force

The data for axial force in Figure 5-32 is essentially the same as seen for lift. This should be expected because lift is the driving force when it comes to rotating the blades, also referred to as the force normal to the blade.

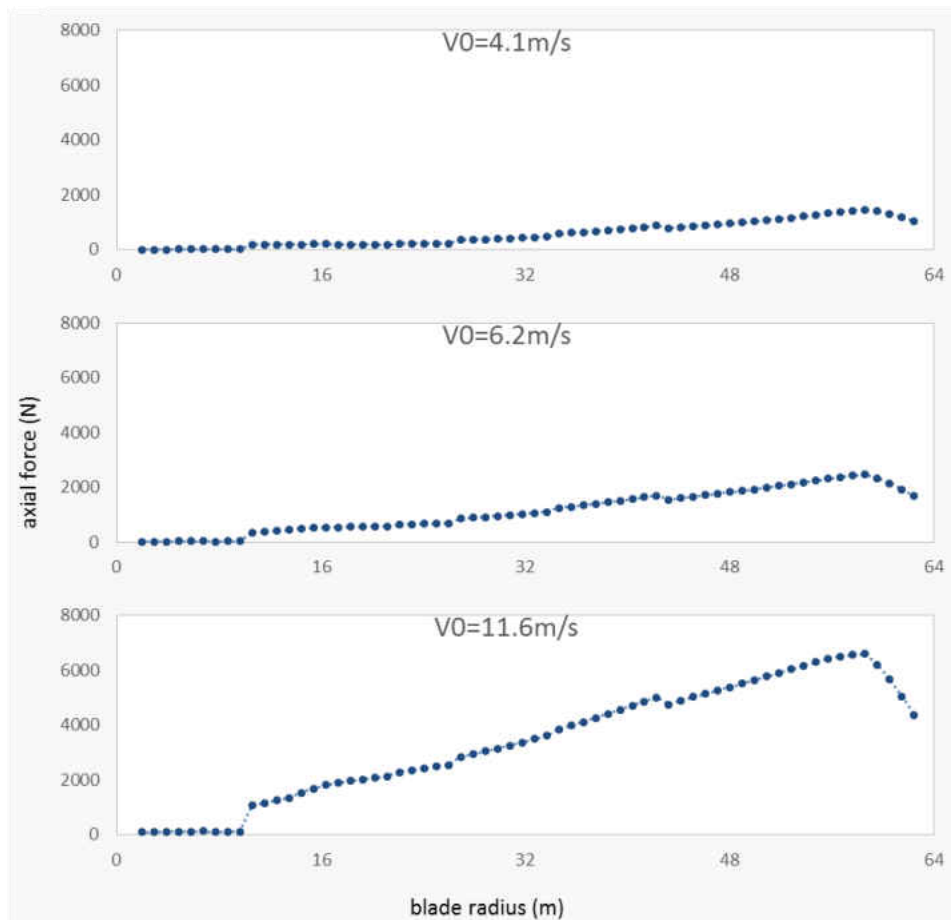


Figure 5-32. Computed averaged axial force along blade

As expected, axial force (Figure 5-33) looks very similar to lift (Figure 5-31).

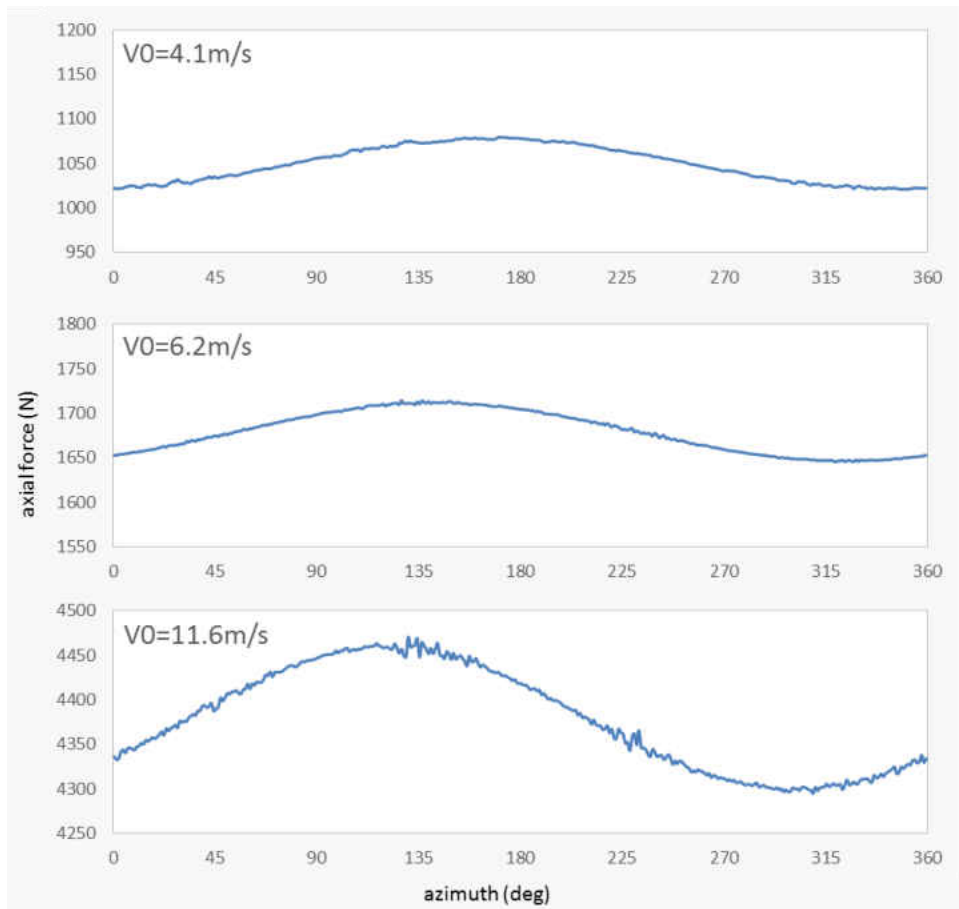


Figure 5-33. Computed axial force of blade tip averaged along azimuth

5.2.10 Tangential Force

For the tangential force in Figure 5-34, there is a group of points that fall in the negatives. If looking closely at the negative values, they are grouped together similar to the data for drag. This shows that the tangential force is along the blade itself and causes a moment at the root of the blade. This is also where drag is greater than lift.

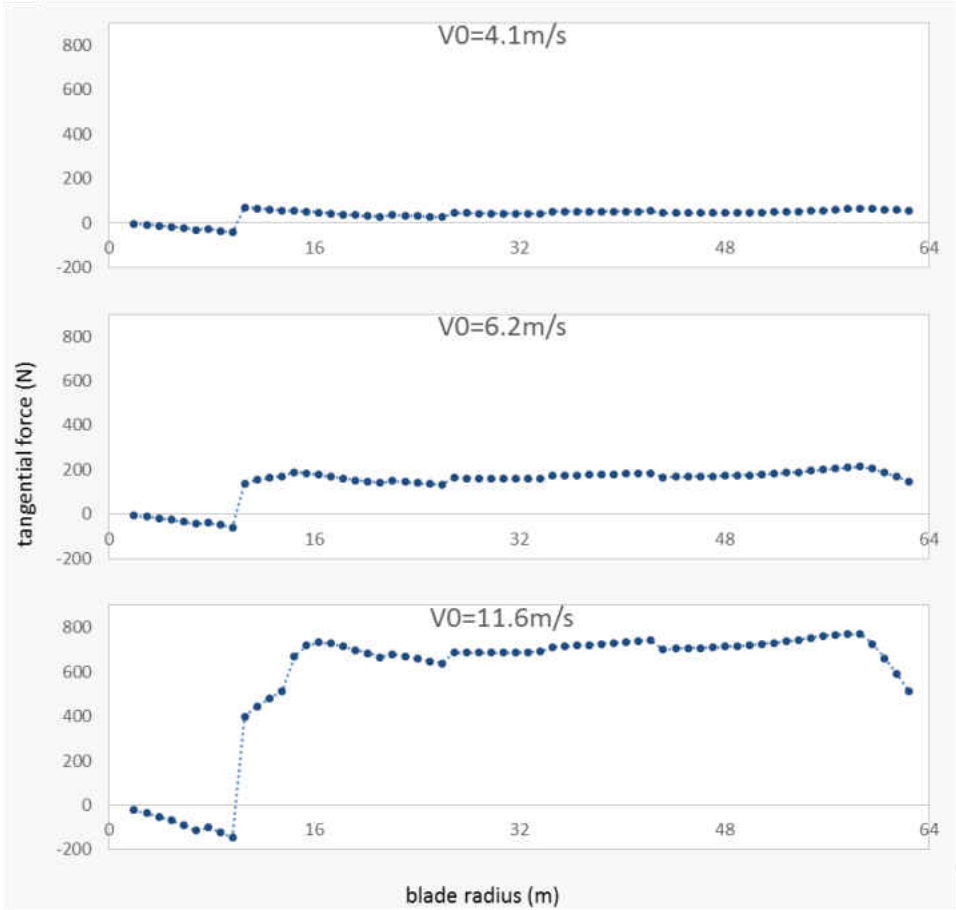


Figure 5-34. Computed averaged tangential force along blade

In Figure 5-35 the tangential force is greatest when it is at the bottom of its rotation. This looks like it matches with axial velocity in Figure 5-15.

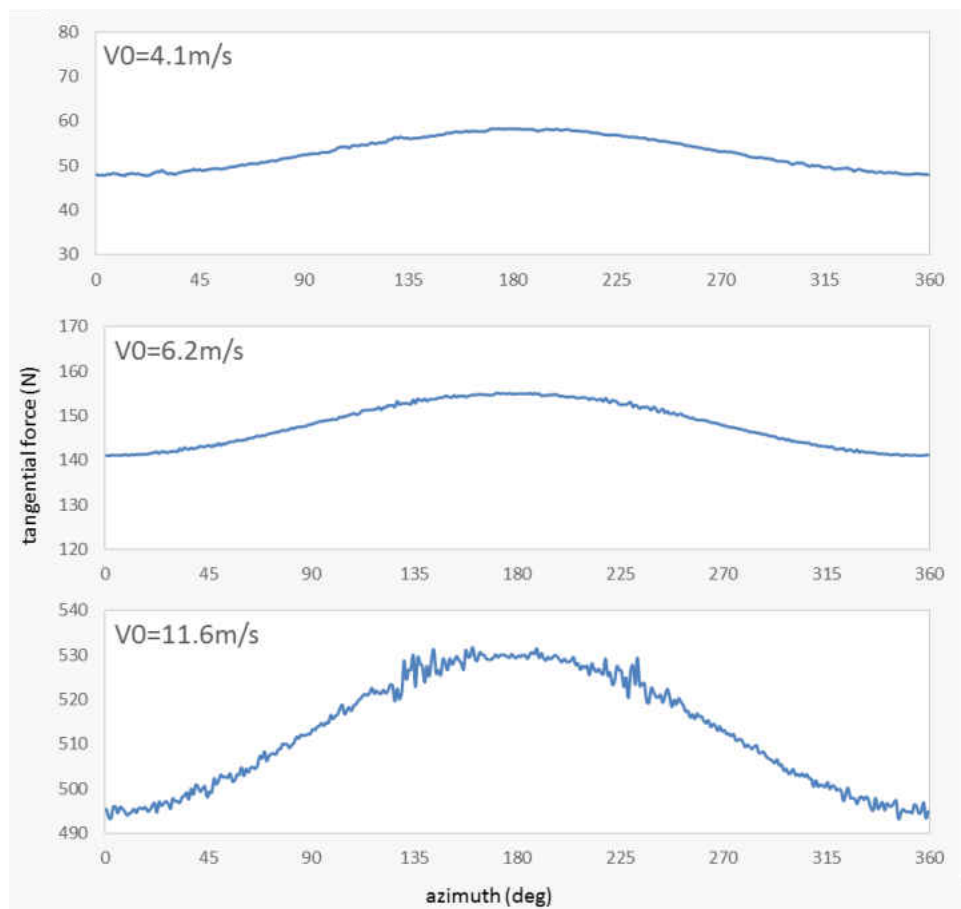


Figure 5-35. Computed tangential force of blade tip averaged along azimuth

5.2.11 Power Generator

Now, in Figure 5-36, compare the power generated to the Equation 2.1.1 to see if the simulated data matched with the expected values. Peak power coefficient $C_p = 0.482$ [7], air density $\rho = 1.225$, and $A = 12445m^2$. The electrical generator efficiency is 94.4%. With these values, the expected power generated would be around 0.23 MW and 0.82 MW. As for anything above 11.4m/s, the power generated will be around 5MW. These calculated values are represented by the red dotted line in Figure 5-36.

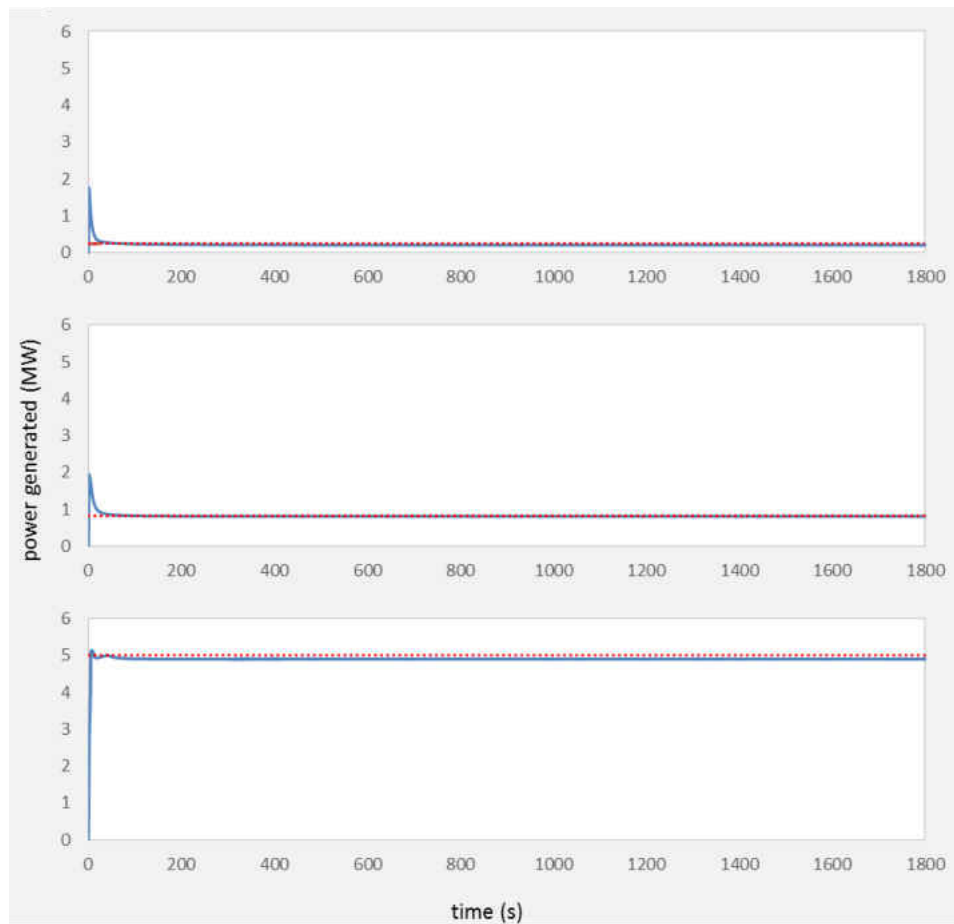


Figure 5-36. Computed power generated over time

A closer look using Figure 5-37 shows that there is some fluctuation for the power generated even though it is relatively small compared to the power generated.

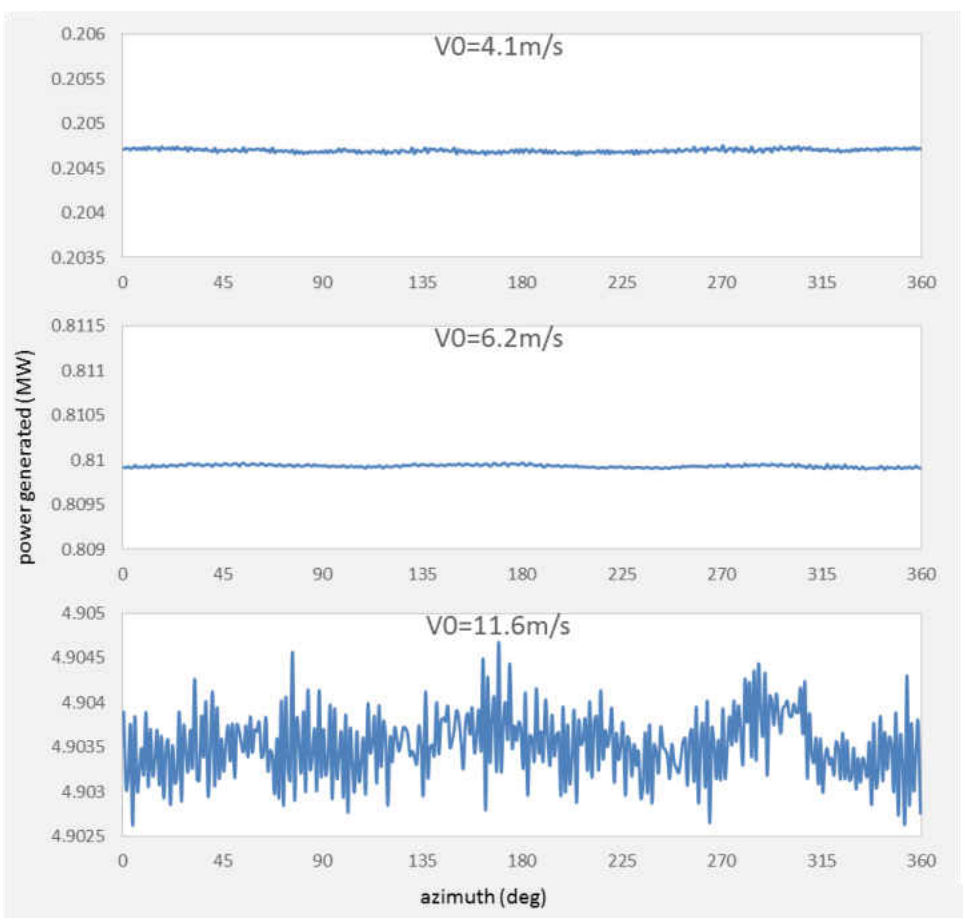


Figure 5-37. Power generated averaged along azimuth

Now, using the average generated power of the turbine and comparing it to the average total power available in the wind, the power efficiency can be determined at each separate simulation as shown in Table 5-1. Peak power for coefficient $C_p = 0.482$ is not exceeded in these simulations.

Table 5-1

Inflow Velocity	Average Wind Power (MW)	Average Generated Power (MW)	C_p
$V_0 = 4.1 \text{ m/s}$	0.53	0.21	0.40
$V_0 = 6.2 \text{ m/s}$	1.82	0.82	0.45
$V_0 = 11.6 \text{ m/s}$	11.95	4.90	0.41

5.2.12 Wake Profiles

Figure 5-38, Figure 5-39, and Figure 5-40 show the axial velocity distribution in the wake for the three simulated cases. The distributions are averaged in time and measured across the horizontal plane (y-axis). The figures below are measured by the axial velocity over the inflow velocity and the distance is measured in terms of radius of blades. In these figures, the values were taken at 3, 6, 10, and 14 radii downstream of the turbine. In the leading plot are the values taken at the blade.

For Figure 5-38, there is a rapid wake expansion immediately after the rotor and the velocity deficit seems to reach near its peak around 3 radii downstream. Somewhere before 10 radii downstream turbulent mixing causes the velocity distribution to become similar to a Gaussian type of distribution.

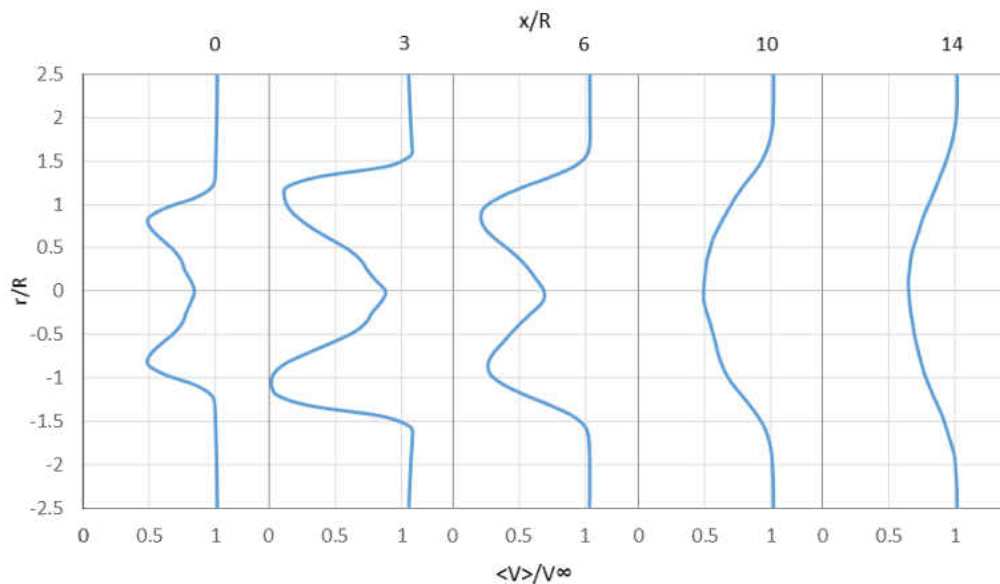


Figure 5-38. Turbine wake profile at constant inflow of 4.1m/s

In Figure 5-39, the distribution expands at a slower rate than the previous figure but is still at a moderate pace. At some point between 6 and 10 radii downstream, the velocity deficit reaches its maximum and is around twice the induced velocities at the blades. At 14 radii downstream, the wake looks like it is developing towards a Gaussian like shape.

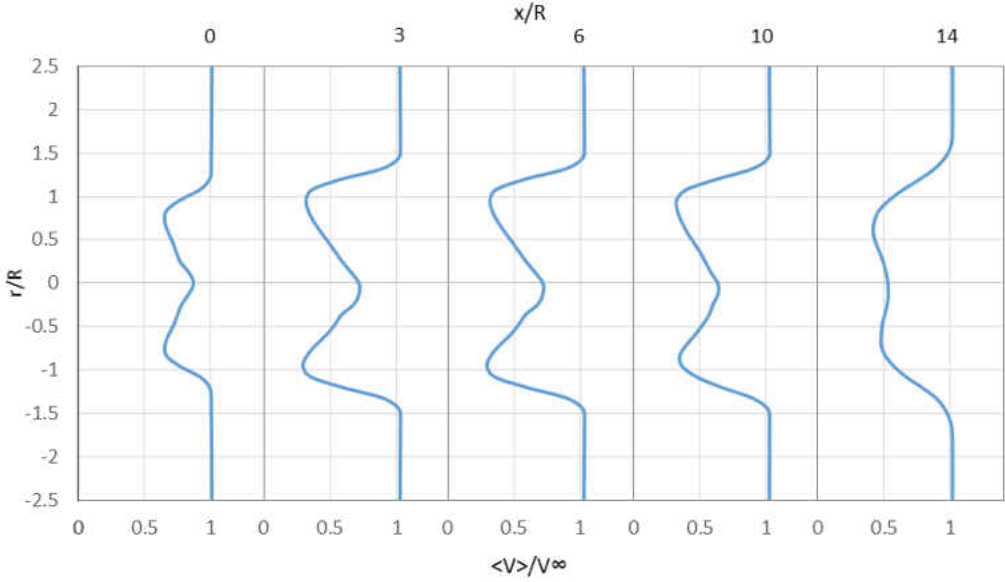


Figure 5-39. Turbine wake profile at constant inflow of 6.2m/s

In Figure 5-40, the wake stays mostly constant downstream, and the axial induction has values close to double the amount than it does at the rotor. In this figure the wake keeps a pretty well defined stream-tube downstream.

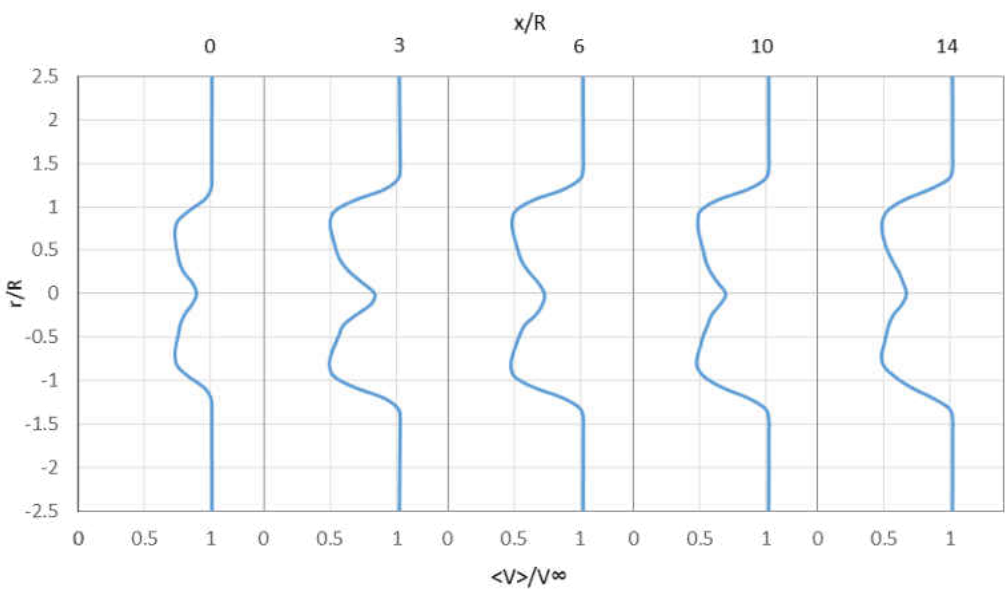


Figure 5-40. Turbine wake profile at constant inflow of 11.6m/s

5.3 Wind Plant

The Wind Plant simulation uses the data produced from the precursor simulation as the inflow for the turbine simulation. The large domain allows for the placement of multiple turbines in specified locations. In this case, there was only one turbine placed in the middle of the domain as seen in Figure 5-41. The image of the left is the time-average velocity magnitude while the image on the right is the velocity magnitude at $t = 22,800$. These data can be compared to the previous turbine data that uses a constant inflow.

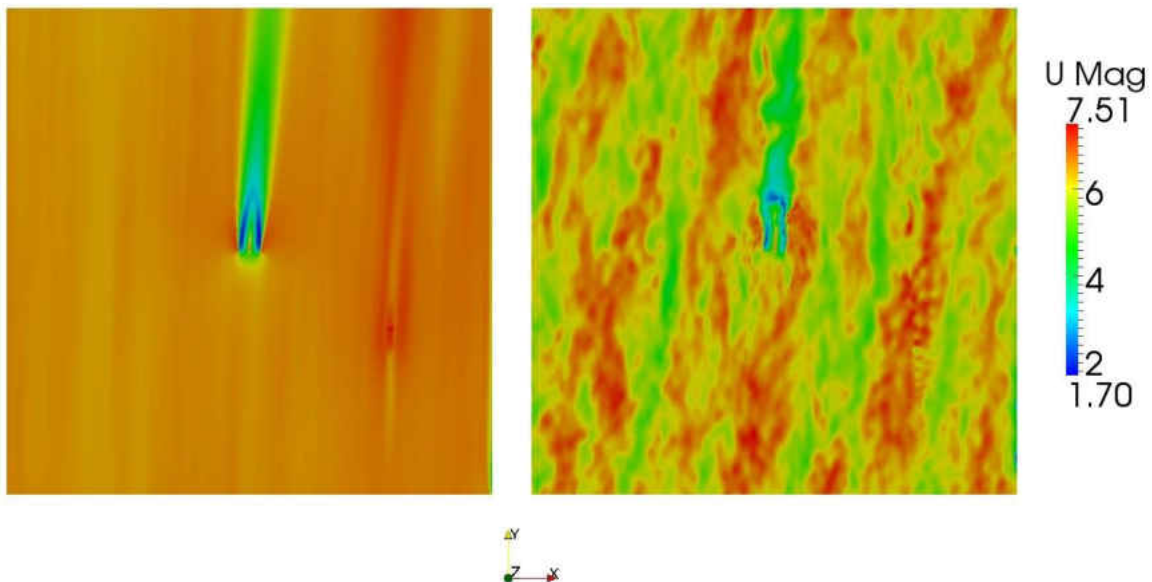


Figure 5-41. Contours of Wind plant simulation for velocity 5.4 m/s

In the figures below, the azimuth for the wind plant data are grouped together by degrees of 3 in order to help smooth out the fluctuations caused by the atmospheric boundary layer, such as the non-uniform inflow. Like in the previous figures grouped by azimuth, the data represent the values near the tip of the blade. As for the data along the blade, the results have very similar shapes as the turbine with the constant inflow.

5.3.1 Axial Velocity

For the wind plant, it can be seen that the axial velocity of Figure 5-42 does not match with the axial velocity in Figure 5-15. This is likely due to the fact that increasing elevation usually increases wind speed. And as seen in Figure 5-42 the lowest velocities on the blade fall near 180 degrees where the tip of the blade is at its lowest and the velocity peak is near the top of its rotation.

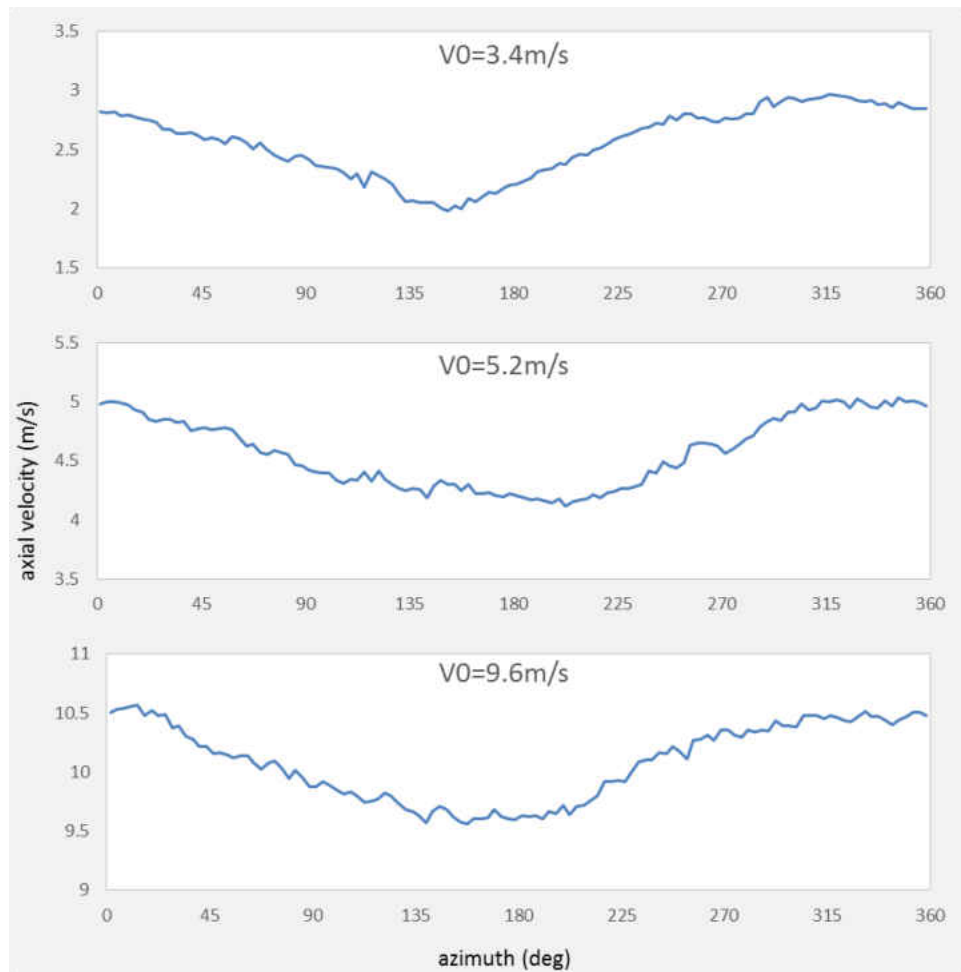


Figure 5-42. Axial velocity of blade tip averaged along azimuth

5.3.2 Alpha

In Figure 5-43, alpha looks like its values correspond to the axial velocity in the previous figure. With this it shows that alpha's relationship to axial velocity are similar in both cases.

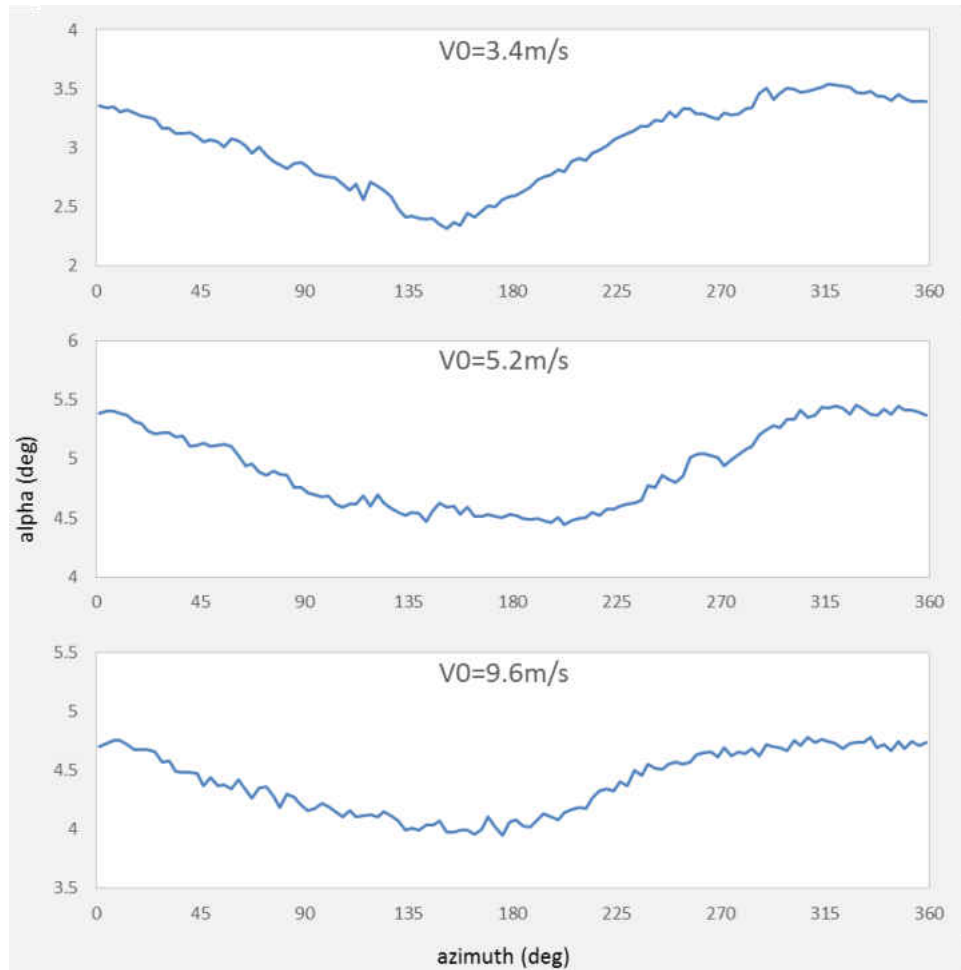


Figure 5-43. Alpha of blade tip averaged along azimuth

5.3.3 Drag

Drag in Figure 5-44 does not seem to have an easy to distinguish pattern. This is most likely caused because the atmospheric boundary layers fluctuations have a pretty large impact on drag since it is a small force respectively.

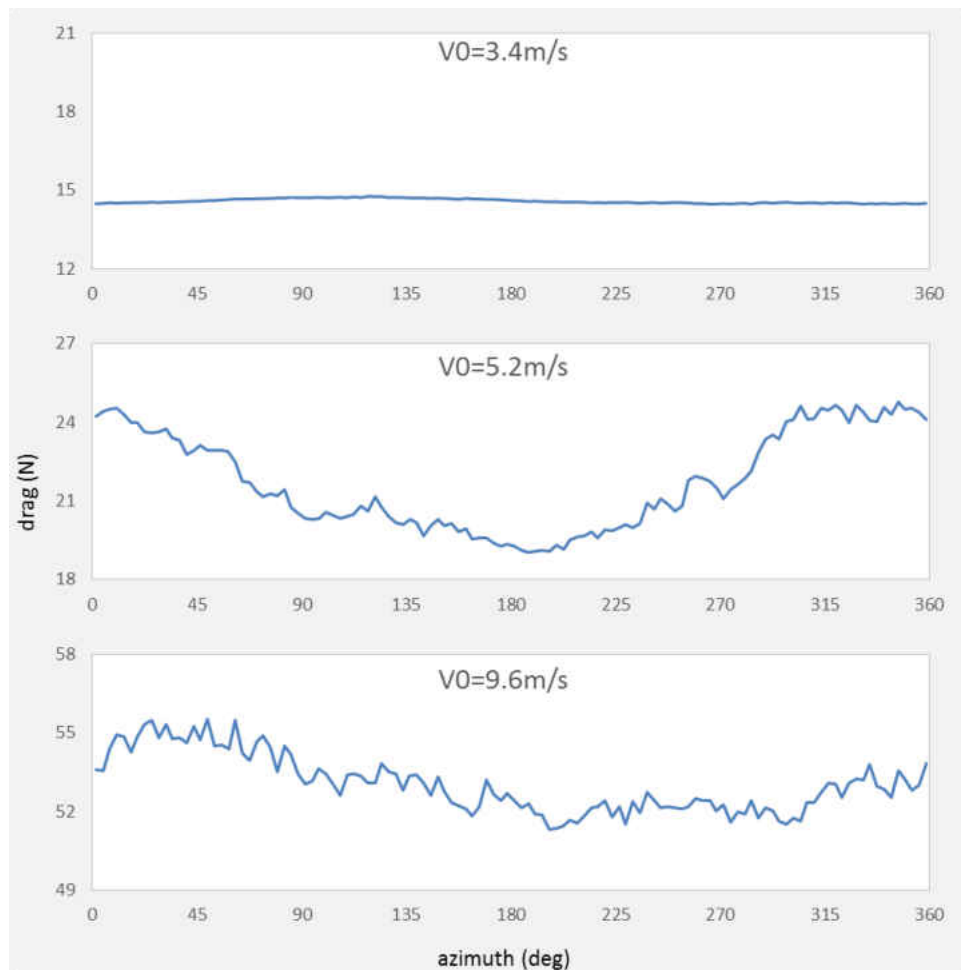


Figure 5-44. Drag of blade tip averaged along azimuth

5.3.4 Lift

Here, lift in Figure 5-45 is correlated again with the axial inflow and resembles a similar pattern. This is expected since lift depend on wind speed which increases with elevation.

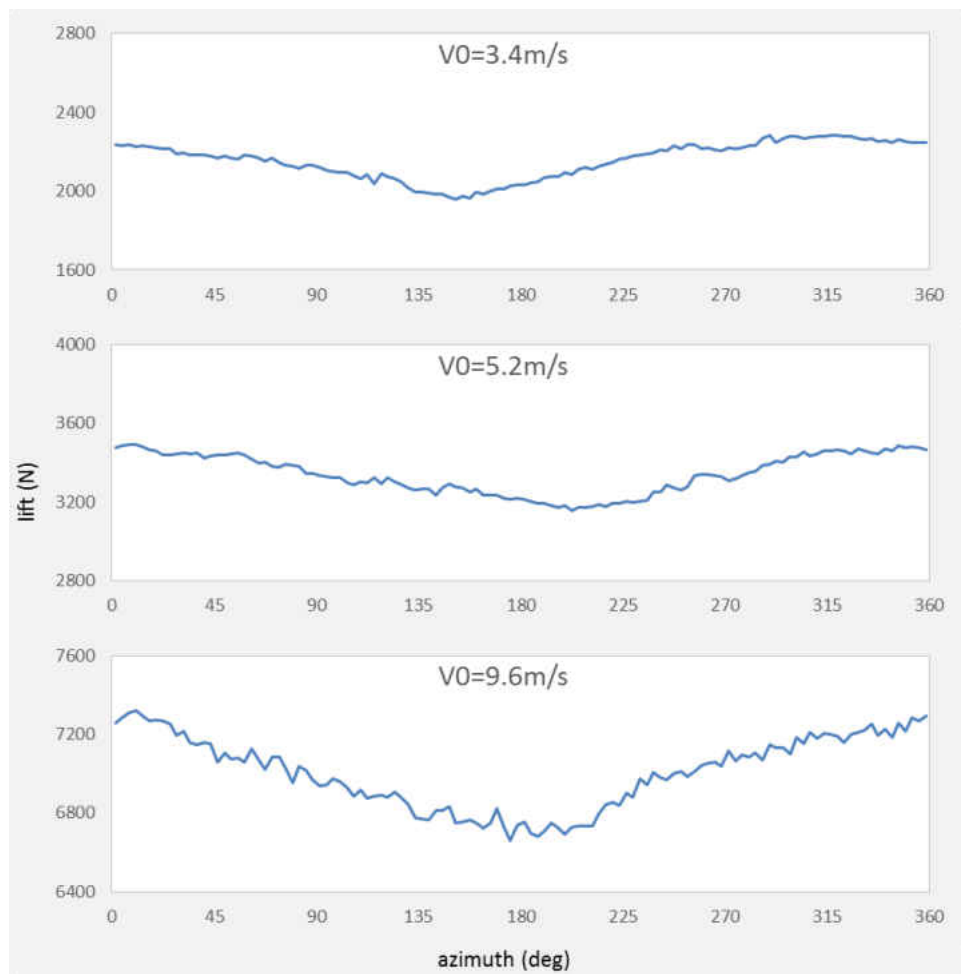


Figure 5-45. Lift of blade tip averaged along azimuth

5.3.5 Power Generator

Figure 5-46 shows the power generated over time for the wind plant simulations. The wind plant simulation for the turbine with the initial velocity of 9.6 m/s reaches the rated velocity at the hub height and averages at about 5 MW. In the two other cases, the average power generated seems to be a little more than in the constant inflow cases of the turbine simulations. The top plot averages at around 0.29 MW, and the bottom plot averages at around 1.1 MW for generated power. The reason for this is because of variability of the wind usually effects the power generated for a turbine. As stated in Chapter 2, gusty sites tend to produce more energy than sites with constant wind speed.

In the cases where the flow used is an ABL shear flow the peak power coefficient does not seem to apply for these simulations. There are circumstances where this can happen like in a simulation using a confined disc in shear flow [31]. Other reasons may be affecting the results such as the grid resolution may have been too course. Though the simulation may need some improvements to get a more accurate power coefficient, there appears to be a clear trend of the turbines being able to extract more wind energy in ABL conditions up until it reaches its rated limit.

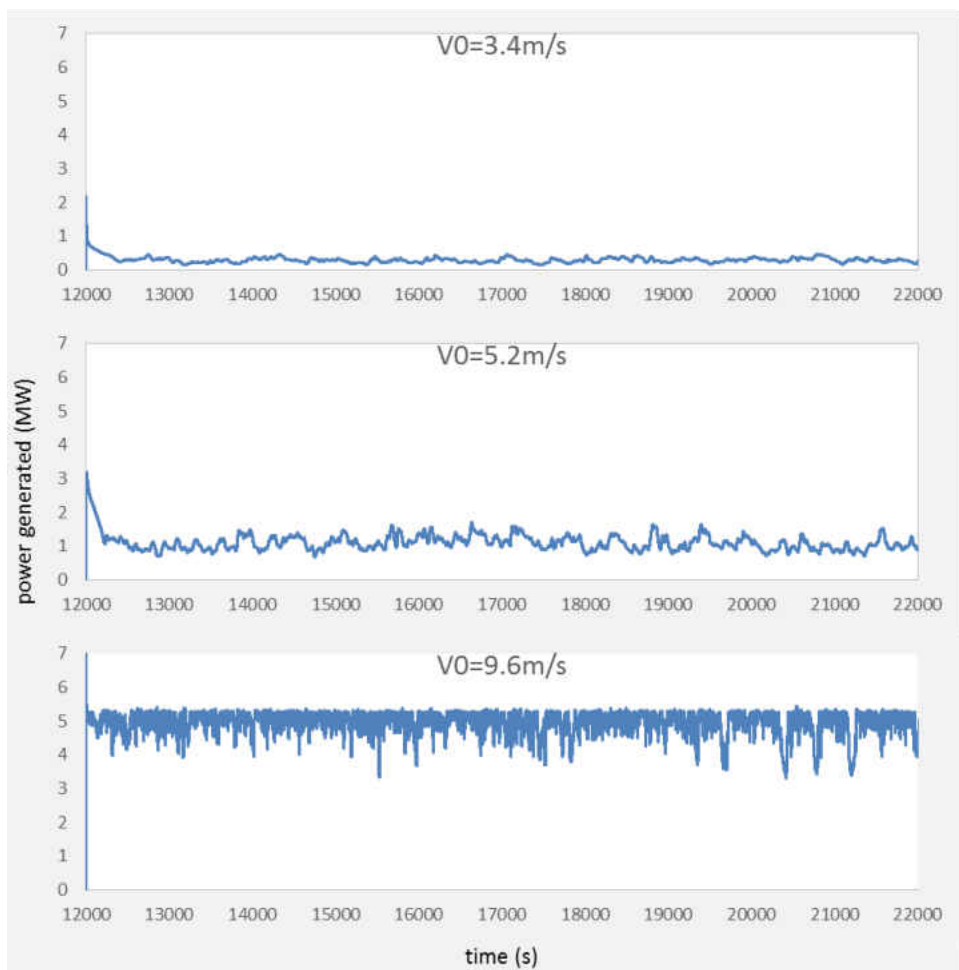


Figure 5-46. Power Generated over time

Table 5-2

Inflow Velocity	Average Wind Power (MW)	Average Generated Power (MW)	C_p
V0 = 3.4 m/s	0.56	0.29	0.52
V0 = 5.2 m/s	1.95	1.1	0.56
V0 = 9.6 m/s	11.8	4.94	0.42

5.3.6 Wake Profiles

The wake in the wind plant simulations have a similar trend to the ones in the turbine simulations. Common trends are that for the slower wind speed the wake expands at a faster rate than that of ones with faster wind speeds. They also follow the turbine simulations in that as the wind speed increases the velocity deficit of the wake also decreases.

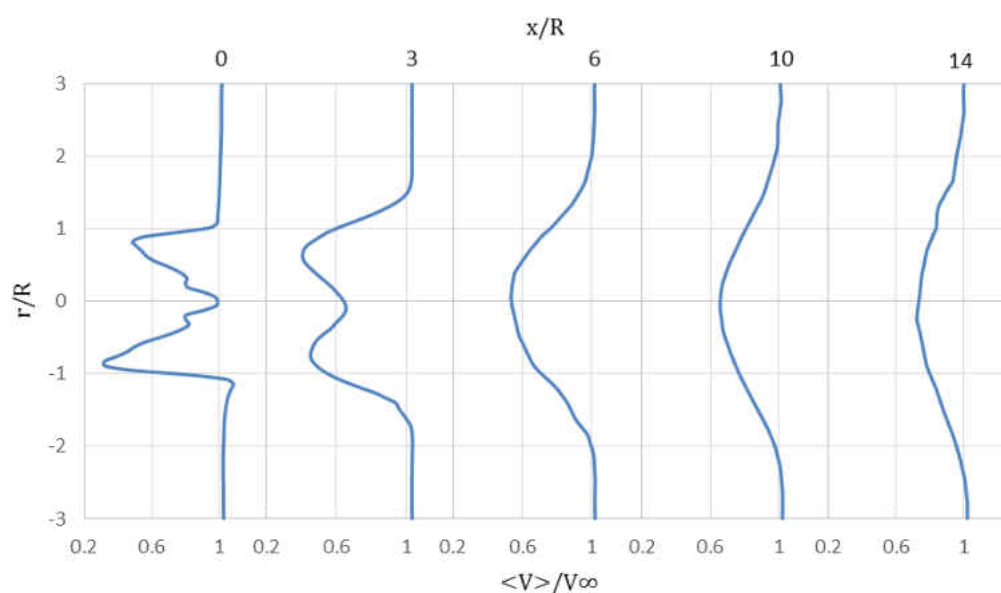


Figure 5-47. Wake profile with velocity of 3.4 m/s with an elevation of 27.9 m

The difference with Figure 5-47, Figure 5-48, and Figure 5-49 from the turbine simulation is that they all seem to reach a Gaussian like distribution by 6 radii downstream. This is mostly like caused from the ABL being more turbulent than the turbine simulation in the constant inflow. This means that the stream-tube will dissipate closer to the rotor plane and allow trailing turbines to gather more energy.

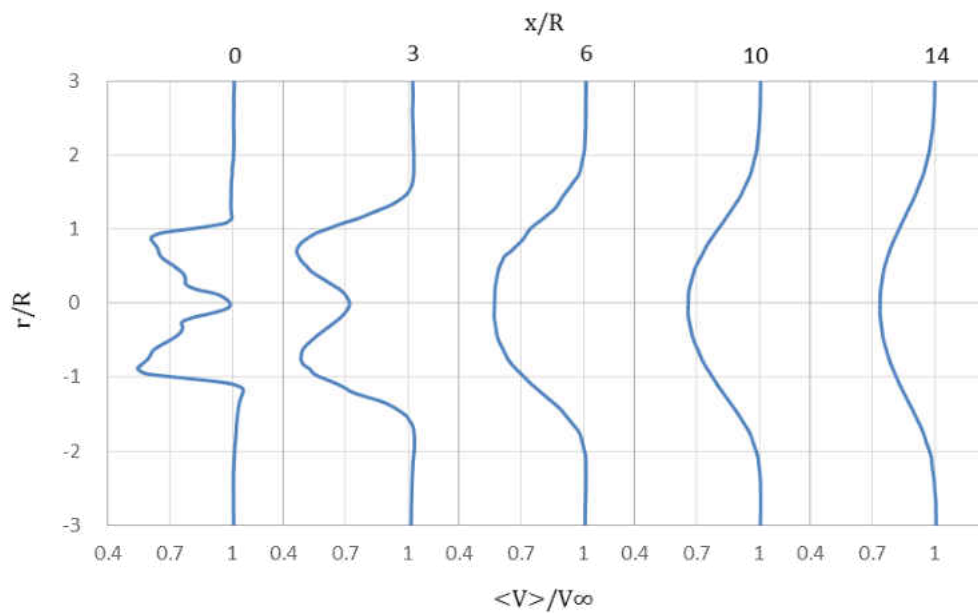


Figure 5-48. Wake profile with velocity of 5.2 m/s with an elevation of 27.9 m

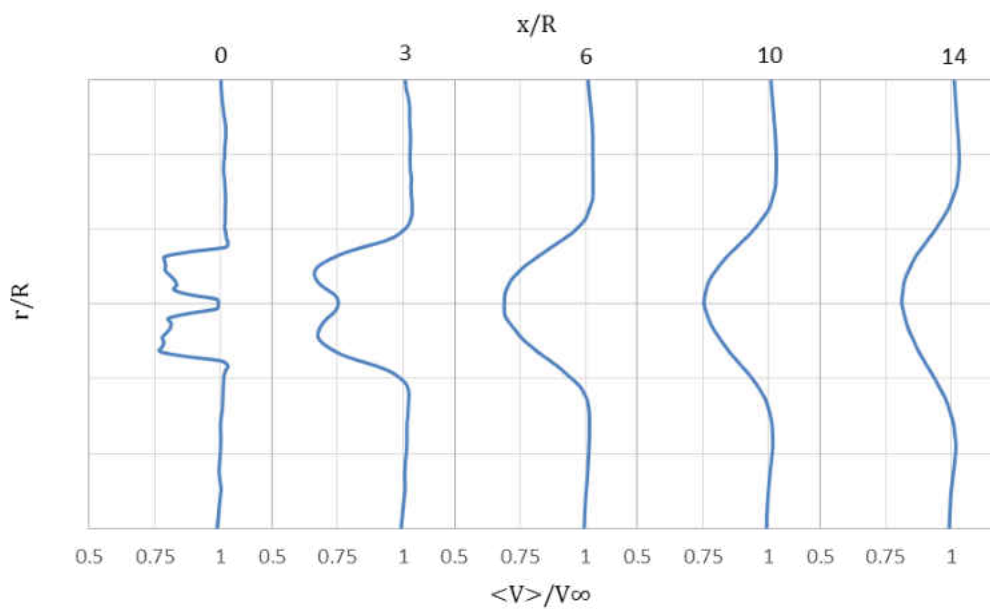


Figure 5-49. Wake profile with velocity of 9.6 m/s with an elevation of 27.9 m

CHAPTER 6

CONCLUSION

With Virginia Beach looking toward using offshore wind as a possible way of generating electricity it is useful to know how much energy a turbine. This gives an idea of how cost effective an offshore wind turbine may be. The study also gives a general idea of the forces acting on the turbine and how the turbine affects the wake. Using local wind conditions can give a more precise estimate than using other test cases of gathered data from other sites.

Gathering local wind data has allowed a better understanding of the wind conditions in the area and can be used to create and estimate for power generation without the use of simulation data. Knowing this can be very helpful in deciding if installing a wind turbine would be reasonable.

Creating the simulations gave a better understanding what was happening at the blades and the types of forces acting on it. It has shown how lift and drag are determined and how they may differ between a turbine in a wind tunnel versus one in an atmospheric boundary layer. Also, seeing the decrease in wind speed in the wake showed how trailing turbines may be affected. An important takeaway is that the simulations created agree with current models and data. Confirming the simulation works in the basic form allows for a move to improve the parameters and create even more specific simulations to the area.

6.1 Improvements

The axial velocity of the wake is important in understanding how leading turbines will create less energy for trailing turbines. A closer look of wake characteristic such as how the tip

vortices and turbulence affect wake and trailing turbines. Trailing turbines not only gather less energy but also deal with more stress from the turbulence caused by the leading turbine. So, in general, knowing more about the wake and its properties would be useful information to understand.

There was also collected data on local gust conditions, which could have been used to create better simulation local to the area

6.2 Suggestions for Future Work

These simulations have a lot of areas that they could expanded and be more specific to the local conditions. For example, the atmospheric boundary layer can use exact data that changes over time. Also, the turbine used was a generic turbine created by NREL and does not simulate the specific turbine that will be used in Virginia Beach. So, in future work, creating an airfoil and blade design that more resembles the planned turbine will generate more accurate data. Additional suggestions for future work include adding more turbine and using variable wind direction.

REFERENCES

- [1] Dominion Energy, "Coastal Virginia Offshore Wind," [Online]. Available: <https://www.dominionenergy.com/coastalwind>. [Accessed 2017].
- [2] Deepwater Wind, "America's First Offshore Wind Farm Powers Up," 12 December 2016. [Online]. Available: <http://dwwind.com/press/americas-first-offshore-wind-farm-powers/>. [Accessed 2017].
- [3] M. Churchfield, S. Lee and P. Moriarty, Overview of the Simulator for Wind Farm Application (SOWFA), National Renewable Energy Laboratory, 2012.
- [4] M. Churchfield, P. Moriarty, G. Vijakumar and J. Brasseur, "Wind Energy-Related Atmospheric Boundary Layer Large-Eddy Simulation Using OpenFOAM," in *19th Symposium on Boundary Layers and Turbulence*, Keystone, 2010.
- [5] T. Burton, D. Sharpe, N. Jenkins and E. Bossanyi, Wind Energy Handbook, John Wiley & Sons, Ltd, 2001, pp. 1-207.
- [6] L. Paul, Onshore and Offshore Wind Energy: An Introduction, John Wiley & Sons, Ltd., 2012.
- [7] J. Jonkman, S. Butterfield, W. Musial and G. Scott, "Definition of a 5-MW Reference Wind Turbine for Offshore System Development," National Renewable Energy Laboratory, Golden, 2009.

- [8] National Data Buoy Center, "Station CHYV2 - Climatic Summary Plots for wind speed," [Online]. Available:
https://www.ndbc.noaa.gov/view_climplot.php?station=chyv2&meas=ws.
- [9] K. E. Armaiz Nolla, "Offshore Wind Energy in the U.S. Mid-Atlantic Region and the EPA Clean Power Plan Proposed Rule," James Madison University, 2014.
- [10] S. D. Baker, "THE ATLANTIC OFFSHORE WIND POWER POTENTIAL IN PJM: A REGIONAL OFFSHORE WIND POWER RESOURCE ASSESSMENT," University of Delaware , 2011.
- [11] S. Christos, *Investigation of the Potential to Implement Offshore Wind Energy Technology in Victoria, Australia*, Uppsala University, 2015.
- [12] M. Churchfield, S. Lee, J. Michalakes and P. Moriarty, "A numerical study of the effects of atmospheric and wake turbulence on wind turbine dynamics," *Journal of Turbulence*, vol. 13, no. 2012, 2012.
- [13] S. Ivanell, "Numerical Computations of Wind Turbine Wakes," Royal Institute of Technology, Stockholm, 2009.
- [14] R. Stevens, D. Gayme and C. Meneveau, "Effect of turbine alignment on the average power output of wind-farms," in *ICOWES2013 Conference*, Lyngby, 2013.
- [15] A. Maselis, "Layout Optimization of Offshore Wind Farms affected by Wake effects, Cable topology and Support Structure variation," Delft University of Technology, 2016.

- [16] E. Quon, M. Churchfield, L. Cheung and S. Kern, "Development of a Wind Plant Large-Eddy Simulation with Measurement-Driven Atmospheric Inflow," NREL, Grapevine, 2017.
- [17] S. Lee, M. Churchfield, P. Moriarty, J. Jonkman and J. Michalakes, "Atmospheric and Wake Turbulence Impacts on Wind Turbine Fatigue Loading," NREL, Tennessee, 2012.
- [18] J. Jonkman, "Dynamics Modeling and Loads Analysis of an Offshore Floating Wind Turbine," NREL, Golden, 2007.
- [19] P. Gebraad, F. Teeuwisse, J. Van Wingerden, P. Fleming, S. Ruben, J. Marden and L. Pao, "Wind plant power optimization through yaw control using a parametric model for wake effects—a CFD simulation study," *Wind Energy*, vol. 19, no. 1, pp. 95-114, 2016.
- [20] H. Namik and K. Stol, "Individual Blade Pitch Control of a Floating Offshore Wind Turbine on a Tension Leg Platform," American Institute of Aeronautics and Astronautics, Aukland, 2010.
- [21] J. N. Sørensen and A. Myken, "Unsteady actuator disc model for horizontal axis wind turbines," *Journal of Wind Engineering & Industrial Aerodynamics*, vol. 39, no. 1-3, pp. 139-149, 1992.
- [22] J. N. Sørensen, W. Shen and X. Munduate, "Analysis of Wake States by a Full-field Actuator Disc Model," *Wind Energy*, vol. 1, no. 2, pp. 73-78, 1998.
- [23] A. Jimenez, A. Crespo, E. Migoya and J. Garcia, "Advances in large-eddy simulation of a wind turbine wake," *The Science of Making Torque from Wind*, vol. 75, no. Journal of Physics: Conference Series, 2007.

- [24] N. Troldborg, J. N. Sørensen and R. F. Mikkelsen, *Actuator Line Modeling of Wind Turbine Wakes*, Lyngby: Technical University of Denmark, 2009.
- [25] J. N. Sørensen and W. Z. Shen, "Numerical Modeling of Wind Turbine Wakes," *Journal of Fluids Engineering*, vol. 124, pp. 393-399, 2002.
- [26] W. Musial, S. Butterfield and A. Boone, "Feasibility of Floating Platform Systems for Wind Turbines," in *23rd ASME Wind Energy*, Reno, 2004.
- [27] National Data Buoy Center, "Station CHYV2 - 8638999 - Cape Henry, VA," [Online]. Available: https://www.ndbc.noaa.gov/station_page.php?station=CHYV2. [Accessed 2017].
- [28] National Data Buoy Center, "Measurement Description and Units," NOAA, [Online]. Available: <https://www.ndbc.noaa.gov/measdes.shtml>. [Accessed 2017].
- [29] National Data Buoy Center, "What averaging procedures are performed on the wind measurements?," [Online]. Available: <https://www.ndbc.noaa.gov/wndav.shtml>. [Accessed 2017].
- [30] The European Wind Energy Association, "Wind Energy Frequently Asked Questions," [Online]. Available: <http://www.ewea.org/wind-energy-basics/faq/>. [Accessed 2017].
- [31] S. Draper, T. Nishino and T. Adcock, "Turbine Blockage in Non-Uniform Flow," in *19th Australasian Fluid Mechanics Conference*, Melbourne, 2014.
- [32] J. Manweill and J. McGowan, *Wind Energy Explained*, John Wiley & Sons, 2009.

APPENDIX A
Airfoil properties

Table A-1. Cylinder1

alpha	C_l	C_d
-180	0	0.5
0	0	0.5
180	0	0.5

Table A-2 Cylinder2

alpha	C_l	C_d
-180	0	0.35
0	0	0.35
180	0	0.35

The remaining airfoils have similar tables that go from -180 to 180 but have a large amount of reference points. The remaining airfoils can be shown in Figure A-1 through Figure A-6

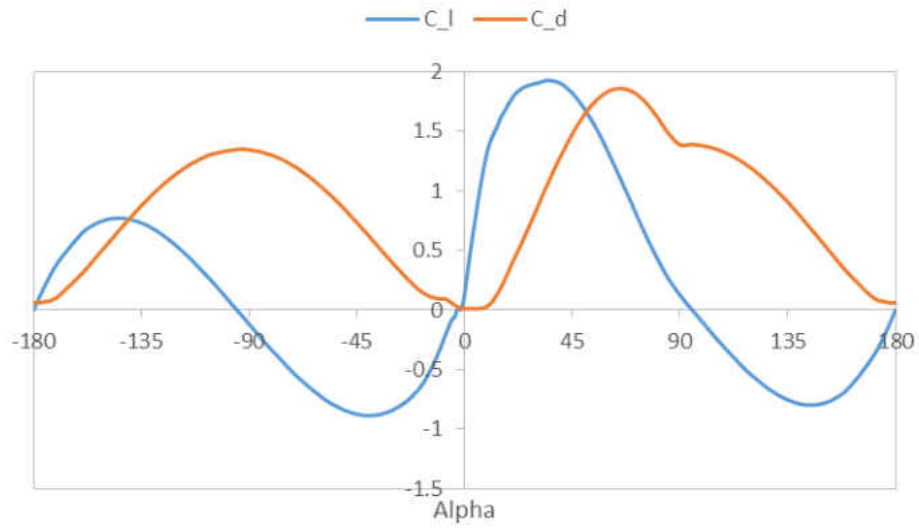


Figure A-1. DU40_A17

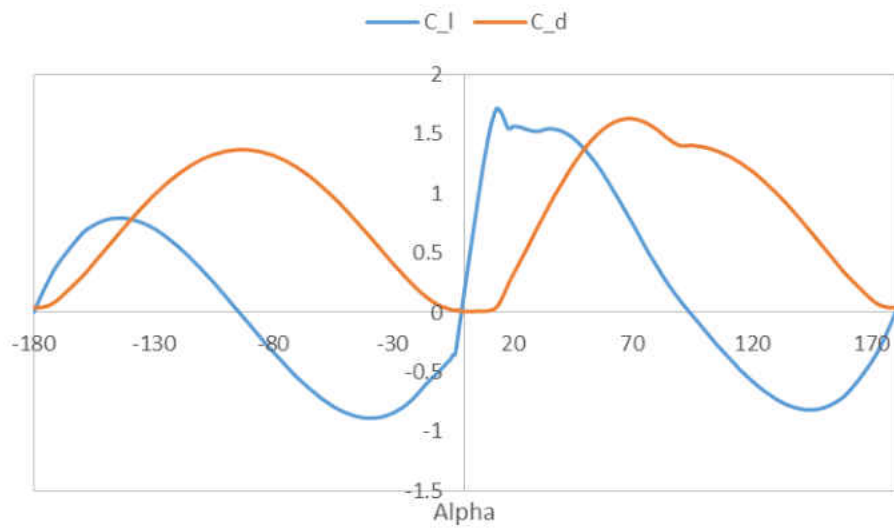


Figure A-2. DU35_A17

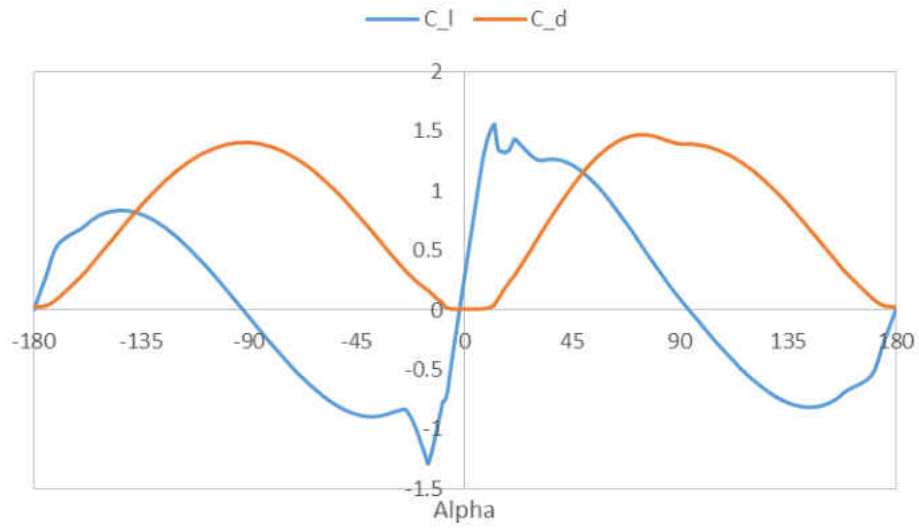


Figure A-3. DU30_A17

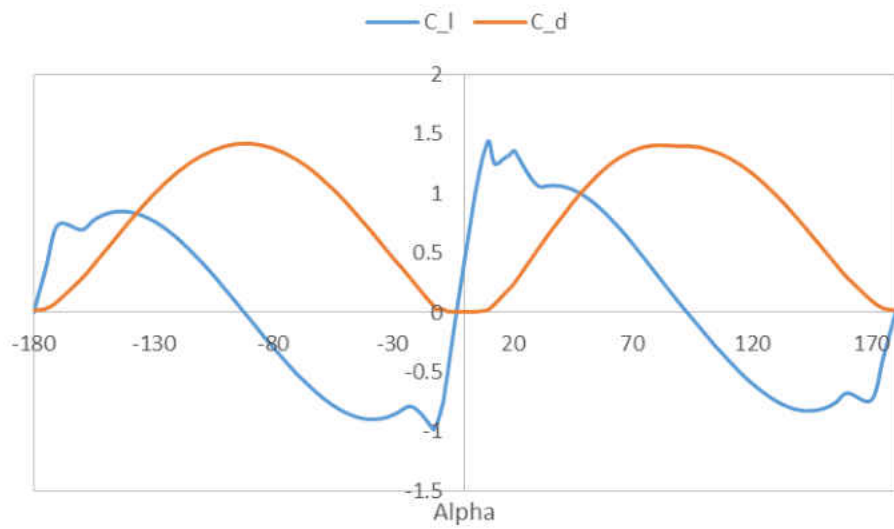


Figure A-4. DU25_A17

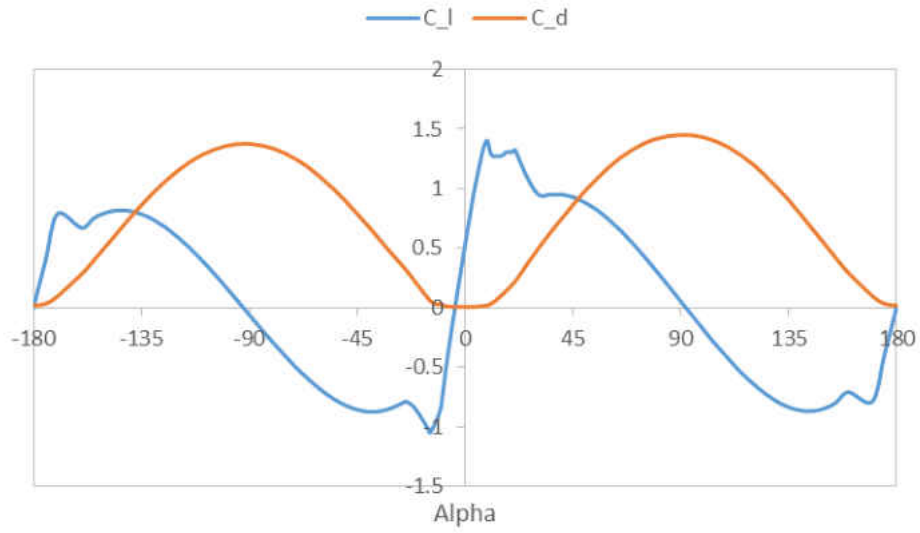


Figure A-5. DU21_A17

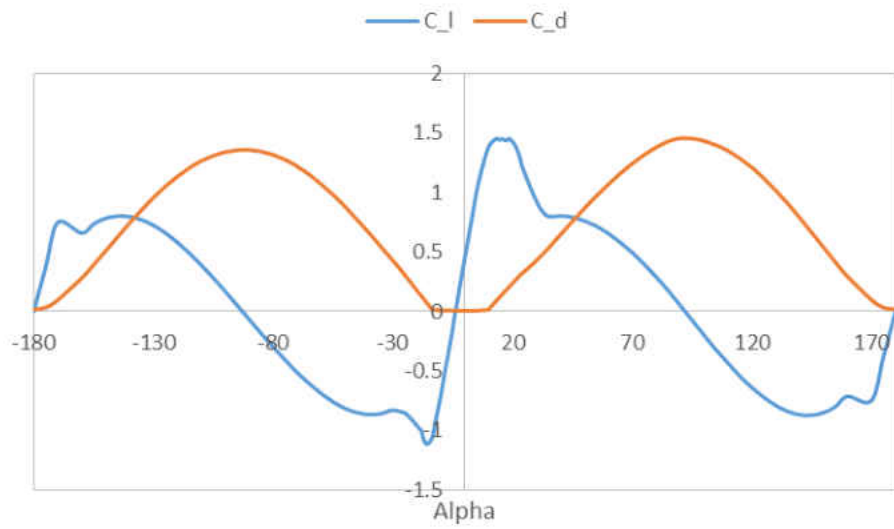


Figure A-6. NACA64_A17

VITA
Ian P. Aquino

Department of Mechanical and Aerospace Engineering
Old Dominion University
Norfolk, VA 23529
(757) 683-5344 (fax); (757) 683-6363 (phone)

Education

M.S	Old Dominion University, Mechanical Engineering	December, 2018
B.S	Radford University, Physics	May, 2011